Preprint of article about an open hardware RTU device.

Multiple Sensor Interface by the same hardware to USB and serial connection

David Nuno G. da Silva S. Quelhas *
Preprint submitted to 'arXiv', December 24, 2024

Abstract

The Multiple Sensor Interface is a simple sensor interface that works with USB, RS485 and GPIO. It allows one to make measurements using a variety of sensors based on the change of inductance, resistance, capacitance, and frequency using the same connector and same electronic interface circuit between the sensor and the microcontroller. The same device also provides some additional connectors for small voltage measurement. Any sensors used for the measurement of distinct phenomena can be used if the sensor output is based on inductance, resistance, capacitance or frequency within the measurement range of the device, obtaining a variable precision depending on the used sensor. The device presented is not meant for precise or accurate measurements. It is meant to be a reusable hardware that can be adapted/configured to a varied number of distinct situations, providing, to the user, more freedom in sensor selection as well as more options for device/system maintenance or reuse.

Keywords: Sensors; Oscillators; Negative capacitance; Design aiming for reuse, repurpose, repair, customization.

1 Introduction

The electronic waste (e-waste) is a modern problem under increasing concern and awareness, there are various possible approaches to reduce and mitigate it, the most obvious is the collection and recycling of discarded devices, however the most ideal is just to make technology that lasts because not only is physically fit by quality design, production, and components; but because its design was intended to be most versatile ensuring the same device can be used and reused in various applications/contexts just by changing connections, jumpers, and firmware configurations. Some design aspects for making a device more reusable are: the use of standard connectors and protocols, think of it as a module to be part of a larger system, minimize barriers for connecting/interfacing components and devices from distinct manufacturers.

1.1 Project objectives and trade-offs

This article is focused on the design of a sensor interface device with USB and serial(UART,RS-485), aimed to allow the interface to many distinct 2-wire sensors based on the change of inductance, resistance, capacitance, frequency, and also small voltage; sensors that can be interchanged using the same hardware and same port of the device, thus meaning the electronics designed must also be versatile.

Providing a versatile device to the users will probably have its negative trade-offs, like:
1- probably significant lower precision/accuracy;
2- some sensor calibration must be provided/done by the end user after replacing a sensor;
3- the calibration function will not be linear or 'easy' as desired for sensors and its interfaces.

However, for some applications the mentioned trade-offs are not necessarily a deal-breaker, such as when the user is technical and is ok with using a device that requires more setup/configuration, some users like devices that are more customizable or repairable. Also is possibly valued a device that if no longer useful for a user, it might still be useful for another user on a different application/context.

1.2 License and context

The hardware design here disclosed is distributed under "CERN Open Hardware Licence Version 2 - Weakly Reciprocal" (CERN-OHL-W), its associated software/firmware under GNU licenses (GPL, LGPL).

This article is about a 'hobby' project done by the author (David Nuno Quelhas, MSc Electronics Eng, alumni of Instituto Superior Tecnico, Portugal) with occasional 'work' between the years 2012 and 2024 on his 'free time'.

1.3 Prior art review

The topic and devices commonly described in literature as 'Multiple Sensor Interface' and also as 'Universal Sensor Interface', commonly fall under 3 distinct categories: a) Device that has a more versatile interface or signal conditioning circuit capable of interfacing various sensor types; b) Device that includes various specialized interfaces or signal conditioning circuits for each sensor type, typically built using various PCB boards for the sensors, to connect or stack into a PCB board with a microcontroller that will register and/or transmit the measurements, or alternatively have all these different circuits integrated inside a single integrated circuit (micro-chip); c) Hardware and/or software systems that collect or register sensor data from various distinct sensing devices/circuits, that may apply some processing to the raw data for obtaining measurements, then to be transmitted to other systems or to a data storage, and so these hardware/software systems may also be called/named 'interface'.

*Lisboa, Portugal; E-mail: david.n.quelhas@gmail.com
https://www.linkedin.com/in/dquelhas
ORCID: 0000-0002-0282-0972
https://multiple-sensor-interface.blogspot.com

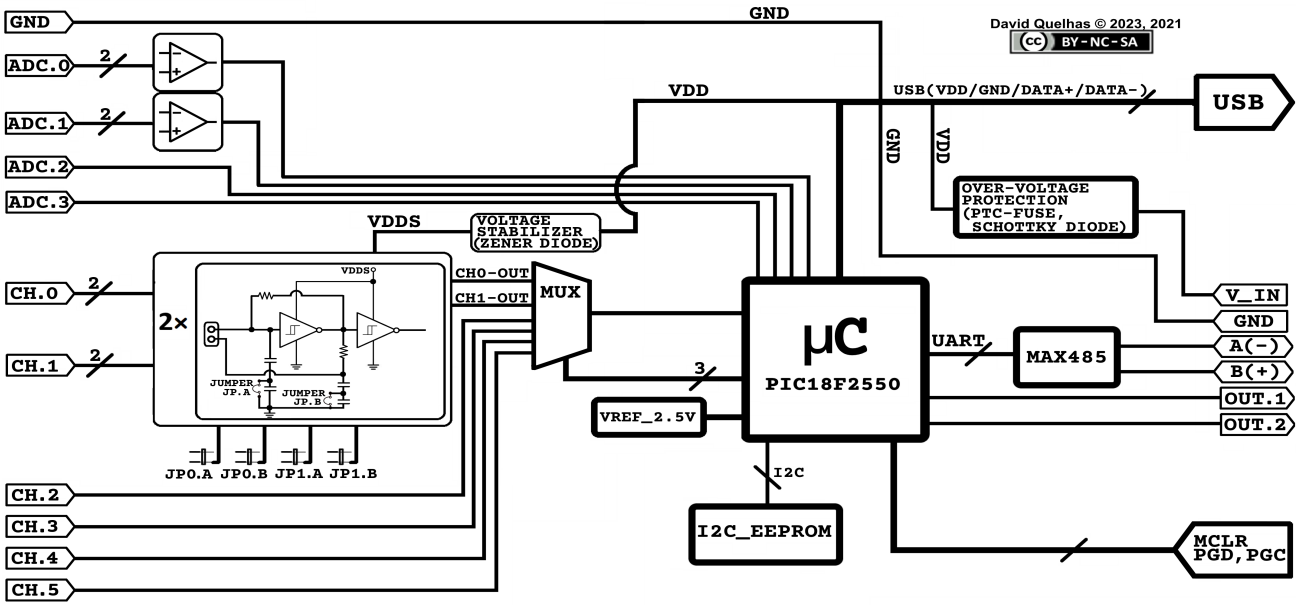

Figure 1: Diagram of the Multiple Sensor Interface device.

The article review presented here is about a 'more versatile interface or signal conditioning circuit' which is the category most similar to this article. Types of versatile sensor interface found in prior art:

1- Interfacing resistive or capacitive sensors by measuring the charge-discharge time of an RC circuit, or measuring the frequency or PWM from an oscillator whose pace is controlled by the speed of a capacitor charge-discharge through a resistor; for example: [7], [8], [9] .

2- Interfacing sensors based on the variation of impedance (includes sensor based on variation of resistance, capacitance or inductance) by an LCR meter, impedance meter, or potentiostat circuit; for example: [10], [11], [12], [13] .

3- Interfacing a sensor as part of a bridge circuit (example: resistive sensor on a resistance bridge, capacitive sensor on a capacitance bridge) [14] .

The Multiple Sensor Interface presented in this article has a working principle more similar to the circuits mentioned as type 1 (RC time or frequency or PWM of oscillator), however in comparison with the mentioned references/articles, the interface circuit of this article can interface more distinct sensor types, namely besides interfacing resistive and capacitive sensors it also interfaces inductive sensors and sensors by frequency measurement using exactly the same circuit and connector/port, also it is a simple circuit with a reduced number of components.

The Multiple Sensor Interface presented in this article in comparison to the circuits mentioned as type 2 (LCR or impedance meters), has the advantage of not requiring an AC voltage/signal generator for exciting the measurement circuit, and not requiring the complex hardware and/or complex post processing for digitizing voltage signal waveforms, that is typically required for the calculation of amplitude and phase difference of voltage signals, on the measurement of impedance by LCR or impedance meters.

The Multiple Sensor Interface presented in this article in comparison to the circuits mentioned as type 3 (measuring a sensor as part of a bridge), has the advantage of using the same circuit for all sensor types (resistive, capacitive, inductive, frequency), instead of requiring a different circuit (the bridge circuit) for each sensor type; thus the interface circuit of this article is a simple circuit with a reduced number of components probably much simpler than any circuitry required for obtaining a single output signal usable for measuring various sensor types on multiple bridge circuits.

A comparison regarding the accuracy or precision of this sensor interface and other interfaces/devices was not made, since the stated focus of the article is how to achieve a most versatile sensor interface, and also considering that such comparison may be easier when considering specific type(s) of sensor/application.

Also regarding a possible use case of the Multiple-Sensor interface presented in this article, where is possible/allowed that an end-user can replace/change a sensor component while maintaining the sensor interface, probably without a sensor calibration; this device is not meant as a measurement device, but as a sensor interface that can provide only qualitative measurements. Example of a qualitative scale (0 to 6 levels) for light intensity [24] : 0- Total starlight (0.0001 lux), 1- Full moon (1 lux), 2- Hallways in office buildings (80 lux), 3- Office lighting (300-500 lux), 4- Overcast day (1000 lux), 5- Full daylight (10000-25000 lux), 6- Direct sunlight (32000-130000 lux) .

2 Design, Materials and Methods

2.1 Sensor Interface Device

Here is presented the Multiple Sensor Interface (Fig.1), the interface main components / sub-circuits are: The connectors and sensor interface circuits (oscillators) for inductance, resistance, capacitance, and frequency (CH.0, CH.1); the connectors and over-voltage protection(zener diode) for frequency measurement (CH.2, CH.3, CH.4, CH.5); the connectors and interface circuit for voltage measurement (ADC.0, ADC.1, ADC.2, ADC.3); analog multiplexer for the sensor channels, the microcontroller (PIC18F2550); I2C EEPROM for storing calibration tables; USB connector; connector and circuit for RS-485 and UART; digital outputs

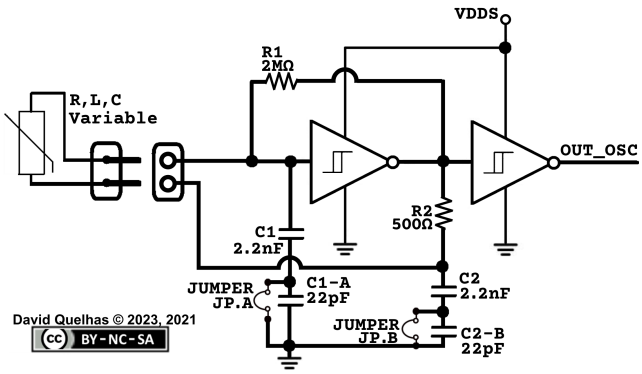

Figure 2: Schematic of the sensor interface circuit (oscillator).

connector (OUT.1, OUT.2).

The digital outputs have the value of a boolean function defined by the user, boolean functions with logic variables that are the result of a comparison ('bigger' or 'smaller' than), between the value/measurement of a sensor channel and a configurable threshold value. The connectors used for frequency measurement may be connected to external single sensor interface circuits (oscillators).

2.2 The sensor interface circuit (oscillator)

The sensor interface (Fig.2) is an oscillator with a circuit design based on the Pierce oscillator with some modifications. The 1st difference is that there is no quartz crystal, and on the location of the crystal will be connected the sensor to be measured (variable inductance or resistance or capacitance), the 2nd difference is that instead of simple inverters ('NOT' gates) will be used Schmitt-trigger inverters(high-speed Si-gate CMOS, 74HC14), this is a very relevant difference that will allow the oscillator to work even with a resistive or capacitive sensor, in fact the interface circuit works with sensors mostly as Schmitt-trigger oscillator. Also the Schmitt-trigger inverters output a noise-free square-wave signal, as oscillator or as external signal converter.

The sensor interface circuit has 2 pairs of series capacitors (C1 2.2nF, C1-A 22pF and C2 2.2nF, C2-B 22pF) instead of just 2 capacitors(C1,C2) so the value of C1 and C2 can be adjusted just by placing/removing a jumper; placing a jumper removes C1-A or C2-B from the circuit making 2.2nF the value of C1 or C2; removing the jumper lets the capacitors in series making 21.78pF the total value of (C1, C1-A) or (C2, C2-B). So on the rest of the article, whenever is mentioned C1 or C2 is meant the resulting capacitor value that can be 2.2nF(jumper on) or 21.78pF(jumper off), accordingly with mentioned jumper configuration.

The sensors can be connected directly on the Multiple-Sensor Interface(on the screw terminals/connectors), or by using a cable; for a cable longer than 20cm is recommended the use of shielded twisted-pair(STP) cable to prevent cross-talk between sensor channels or external EMI.

2.3 Measurement process

The Multiple-Sensor device has a microcontroller (PIC18F2550) that is able to make frequency and voltage measurements, so the device makes frequency measurements for sensor channels CH.0 to CH.5 ; and makes voltage measurements for sensor channels ADC.0 to ADC.3; these frequency and voltage measurements made by the device are designated as the raw_value of a sensor channel. To obtain the measurement of a sensor channel, the device uses a 2 column calibration table, that is a long list of points (raw_value; measurement) relating the measurement value (obtained during calibration by an external reference device) to the corresponding raw_value obtained on the Multiple-Sensor device, these calibration tables are stored on an I2C EEPROM memory on the Multiple-Sensor device.

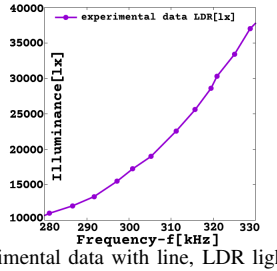

Figure 3: Plot experimental data with line, LDR light(brightness) sensor connected on Multiple-Sensor Interface; example of a calibration table exclusively from experimental data.

The Multiple-Sensor device can work in two modes: single-channel or multiple-channel, the CH.0 to CH.5 raw_value(frequency) are calculated through a counter/timer of the PIC18F2550 by periodically reading its value and calculating the frequency f=count/period ([Hz]=[cycles]/[s]). So in single-channel mode the frequency is always calculated on the selected/enabled sensor channel, in multiple-channel mode the frequency is calculated for each sensor channel sequentially (time-division multiplexing), since there are 6 channels to measure but only on counter/timer of the microcontroller for that job. Thus in multiple-channel mode a measurement takes 6x more time to be updated/refreshed than in single-channel mode.

For the sensor channels ADC.0 to ADC.3 the raw_value is the voltage of those channels measured by using the ADC (Analog to Digital Converter) of the microcontroller and also reading a 2.5V voltage reference.

The sensor measurements are calculated by searching the raw_value on the corresponding calibration table, and by using from the table 2 points (raw_value,measurement) referenced here as points P and Q such that the measured raw_value is bigger than raw_value of P and is lower than raw_value of Q; then is calculated a linear equation: $measurement = a \cdot (\text{raw\_value}) + b$, defined by the points P and Q. So every-time the device calculates a sensor measurement, it will calculate the corresponding linear equation for the current raw_value and use it to obtain the current measurement (Fig.3) .

2.4 Device calibration for a sensor

Device calibration is about obtaining calibration tables for each sensor channel, here are 2 ways to obtain it:

1- Do a full manual calibration using an external meter as reference where both the reference meter and the Multiple-Sensor device(with a sensor connected) are exposed to same stimulus/environment that is controllable by the user to produce all adequate variations/intensities necessary to record an extensive calibration table, with all experimental pairs of (raw_value,measurement).

2- Using a known function that relates the measured phenomena to the obtained raw_value on the Multiple-Sensor device (obtained by theoretical or experimental study), although a purely theoretical calibration could be used, prob-

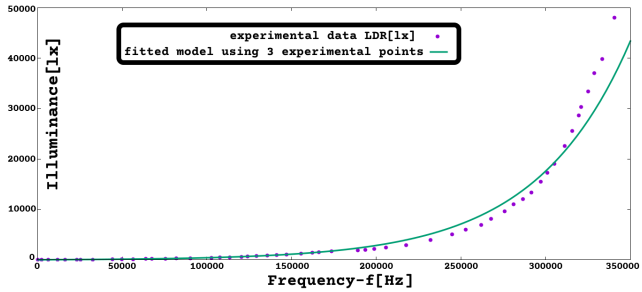

Figure 4: Plot experimental data and fitted model(by using 3 points), LDR light(brightness) sensor connected on Multiple-Sensor Interface.

ably is better or easier to obtain a calibration table by using a known function and have its constants/parameters calculated by a data fitting to some few experimental data points (raw_value, measurement) obtained for the device calibration. So for example if the known function had 3 constants/parameters, it would require at least 3 different experimental measurements to obtain the function for that sensor channel, then having the function is just a question of calculating a longer list of pairs (raw_value,measurement) on the desired measurement range. Fig.4 is the result of fitting the model function $Illuminance(f) = a + b \cdot (e^{c \cdot f})$, to the points: (244Hz, 0.01 [lx]), (25320Hz, 30 [lx]), (232041Hz, 3950 [lx]); obtaining the values: a=−80.2359; b=79.8743; c=$1.79972 \cdot 10^{-5}$. The symbol e is the Euler-Napier constant. The point at 244Hz was changed from 0[lx] to 0.01[lx] as it may facilitate/improve the model function fit.

2.5 Methods for error analysis of Multi-Sensor device

A theoretical analysis of the measurement error of the Multiple-Sensor Interface can be made based on the theoretical results obtained on the following sections, for example by making a comparison between the expected theoretical values of $R_s(f)$, $C_s(f)$, $L_s(f)$ as Schmitt-trigger oscillator and the measured values (experimental data). Also it can be explored the theoretical predictions of how much the uncertainty of each electrical parameter (circuit constants) contributes to the uncertainty of the sensor measurement; that is, how the measurement error theoretical correlates with the error/uncertainty of the electrical parameters of circuit components. A possible method for the theoretical error analysis can be based on the formula of the upper bound of the error propagation, similar to the General Formula for Error Propagation, but always valid regardless from the fact if the errors on independent variables (here the electrical parameters) are independent or random. The formula of the upper bound of the error propagation is: if $q = q(x,...,z)$ is any function of x,...,z, then $\delta q \leqslant |\frac{\partial q}{\partial x}|\delta x + ... + |\frac{\partial q}{\partial z}|\delta z$, [22], [23] .

Also, one typical term/concept for the error analysis of oscillators is the study of the 'frequency stability' ($\Delta f/f$), that commonly is analysed and/or tested against external factors like power supply voltage and temperature. Since the oscillator studied here has the purpose of being a sensor interface, and not the typical purpose as generator of cyclic voltage signal, the analysis focus will be on the measurement error with specific sensor(s) and regarding the interface circuit will be based on the functions $R_s(f)$, $C_s(f)$, $L_s(f)$. Relevant to the error analysis done here is to recognize that variations in temperature and in supply-voltage (V_{DDS}) are interesting to be considered regarding the measurement error (just like variations in R_1, R_2, C_1, C_2). Also, variations in supply-voltage (V_{DDS}) will affect the theoretical measurement error through the H parameter that will be defined in the theoretical analysis as $H = ln\left(\frac{(V_T^- - V_{DDS})V_T^+}{(V_T^+ - V_{DDS})V_T^-}\right)$.

Variations over time of the electrical parameters R_1, R_2, C_1, C_2, contribute to the measurement error; and in case of a calibration based purely on theoretical formulas the tolerance/uncertainty of R_1, R_2, C_1, C_2 will also contribute to the measurement error. The tolerance of the components on the Multiple-Sensor device/PCB, that was used on the experimental work/tests is: ±5% for resistors (R_1, R_2), and ±10% for capacitors (C_1, C_2). By tolerance is meant, the maximum deviation allowed from the specified nominal value of the electrical parameter of a component. On the entire article, the values used for calculating the theoretical results where the nominal values of the components R_1, R_2, C_1, C_2.

The author considers that isn't convenient and/or interesting to include the theoretical (and numeric) prediction of the error (for example using the General Formula for Error Propagation) based on the theoretical analysis (equations of R_s(f), C_s(f), L_s(f)) in the scope of this article, because: 1- Is a calculation intensive process that produces an output that requires a long written content (tables and text) to be presented; 2- the proximity/conformity between experimental data and the theoretical models is already depicted on various graphs available on the article that show both theoretical and experimental data; 3- The presented theoretical analysis is already stated to include some mathematical approximation and so it should be expected some deviation/displacement between the theoretical models and the experimental data.

So a numeric characterization of the measurement error may be more interesting if applied to specific combination of sensor plus the Multiple-Sensor Interface. The characterization of the measurement error that is available on the Appendix sections, is a comparison/difference between large set of experimental data measurements against the values obtained from theoretical models that were fitted with a small subset of experimental data; so these fitted models may be a convenient way to obtain device calibration where is meaningful to analyse the measurement error, and where the known/nominal values of circuit parameters (R_1, R_2, C_1, C_2) and sensor parameters(sensor specific) are used as the initial value of the parameters that are calculated by the model fitting.

On the Appendixes D and F, are graphs of fitted models (for example a theoretical model fitted with 8 samples of experimental data) that where obtained by using the 'fit' command of the GNUPlot software (it applies the "nonlinear least-squares Marquardt-Levenberg algorithm" [15]); also is included/listed the experimental data samples used on the model fitting, the obtained model parameters, and error analysis graphs of the models.

2.5.1 Temperature variation and measurement error

The variation of temperature may influence indirectly the measurement error, as for example, typical room temperature variations are expected to cause small variations of the values/parameters of the resistors and capacitors used on the multiple sensor interface (R_1, R_2, C_1, C_2), and these small

temperature variations if not taken into account on the measurement process, as is the case with basic/inexpensive sensor interfaces like this one, will cause a small increase of the measurement error. More relevant is to check the effect of temperature on the measurement error related with semiconductor devices, like the integrated circuit 74HC14 (Schmitt-trigger inverters) that was used on the sensor interface; since by the physics of semiconductors the relation between resistivity and temperature is given by an exponential function. The only electrical parameters used on the theoretical models of this article related to the Schmitt-trigger inverter are: V_T^-, V_T^+; and the relation of these parameters with temperature can be consulted on the datasheet of the IC used (Nexperia/NXP 74HC14) [17] and on similar hex Schmitt-trigger gates that do have more information/detail on how V_T^-, V_T^+ change versus temperature. The datasheet of 74HC14 by Nexperia/NXP [17], and also datasheets of similar devices like: MC74HC14A by Onsemi [18]; CD40106B [19] and SN74LS14 [20] by Texas Instruments; basically indicate that V_T^-, V_T^+ are nearly constant over the entire operational temperature range, since in parameters tables, they indicate a single value of V_T^- and of V_T^+ for the entire temperature range (-40 ºC to +125 ºC). The datasheet of SN74LS14A by Texas Instruments [20] provides on page 8 a graph showing that the variation of V_T^+ versus temperature and V_T^- versus temperature is minimal (almost constant).

So the overall effect of typical room temperature variations on the Multiple-Sensor interface is of small relevance to the type of low-end (not high precision) applications intended for this device.

2.5.2 V_{DDS} variation and measurement error

The variation of the power supply voltage (V_{DDS}) may influence indirectly the measurement error, since a variation of V_{DDS} is expected to cause a variation of the H parameter that is used on the following theoretical analysis. Also is relevant to notice that in accordance with the tables on the datasheet of the IC used (Nexperia/NXP 74HC14) [17] the values of V_T^-, V_T^+ have significant variation versus the power supply voltage (indicated as V_{CC}). The datasheet of MC74HC14A by Onsemi [18] provides on page 5 a graph showing a linear relation between V_T^+ versus V_{CC} and V_T^- versus V_{CC}. So from the information on the datasheet for the purpose of the measurement error analysis, is appropriate and interesting, to replace the V_T^+ and V_T^- by a function that has V_{DDS} as independent variable, and that would be the most accurate way to study the influence of V_{DDS} on the measurement error. For a measurement error analysis where variations/uncertainty of V_{DDS} are considered, the 'H' parameter will be the only model parameter that is influenced by V_{DDS}, accordingly with the expression $H = ln(((V_T^- - V_{DDS})V_T^+)/((V_T^+ - V_{DDS})V_T^-))$, that will be introduced on the theoretical analysis. Also more information on how the 'H' parameter is influenced by power supply voltage is available on page 9 and 10 of the datasheet of the IC used (Nexperia/NXP 74HC14) [17], where is mentioned the expression $f = 1/T \approx 1/(KRC)$, where the 'K' parameter of the datasheet corresponds to the 'H' parameter of this article, and the RC product of constants corresponds to the $\tau = -1/\lambda$ parameter of this article. On the mentioned datasheet [17] there is plot of $K(V_{CC})$ that is consistent/similar with the $H(V_{DDS})$ expression that was defined in this article.

However, for the sake of simplicity in this article, the values of V_T^+ and V_T^- will be considered as constants on the theoretical analysis, and the error analysis available on the appendix sections doesn't includes/considers the variations/uncertainty of power supply voltage (V_{DDS}).

2.5.3 Suggestions for minimizing the measurement error

A sensor connected on the sensor interface may intentionally be matched with some corresponding values of C_1, C_2 (or also R_1, R_2), for example by a changeable jumper connection, or alternatively adding/connecting a fixed value resistor/capacitor/inductor in parallel with the sensor, to better align the functions $R_s(f)$, or $C_s(f)$, or $L_s(f)$ that define the sensor interface with the values of R_s, or C_s, or L_s expected for the sensor output when measuring whatever dimension/phenomena, maximizing the use of the sections of $R_s(f)$, or $C_s(f)$, or $L_s(f)$ that have the lowest measurement error. Also having components C_1, C_2, R_1, R_2 with lower/better tolerance can give a small contribution for reducing the error between theoretical results and experimental data. Also, it may be possible to obtain fitted functions (of sensor measurement, or of $R_{s,Fit.}(f)$, or $C_{s,Fit.}(f)$, or $L_{s,Fit.}(f)$) with smaller measurement error, by selecting a different set of experimental data to use on the model fitting, or by limiting/reducing the range of values where the calibration is valid/used (and so using for model fitting a narrower set of experimental data that actually is the most relevant for the measurement range of the specific sensor).

3 Results and Analysis

3.1 Device testing

The author developed and built prototypes of the described device, made of the components described in the previous section and in Fig.1 diagram. Then the device was experimented with various different sensors; including various common sensor components, namely: LDR (Light Dependent Resistor or also designated as photo-resistor), RTD(Resistance Temperature Detector), FSR(Force Sensitive Resistor), Relative-Humidity sensor (RH to impedance); also a water level / soil moisture sensor made with 2-layer PCB, and as well some handmade sensors done by the author for the purpose of exploring the device usability, namely: a proximity sensor (based on the variation of inductance of a flat coil, caused by the vicinity of a metallic object, or the vicinity of a non-metallic object covered with aluminium or copper adhesive tape), a force sensor (based on resistance variation when pressed) made using 'carbon impregnated foam' (also known as ESD/antistatic foam), aluminium foil and adhesive tape.

The tests done with the device connected on the various mentioned sensors, were made with the purpose of verifying that the device is indeed usable with various types of sensors, but those tests are not the most appropriate for studying how the device works, or for characterizing the device itself by determining its usability range, or for gathering quantitative data about the device to be used along with the data from a sensor datasheet for determining its compatibility.

So the tests chosen for characterizing the device were

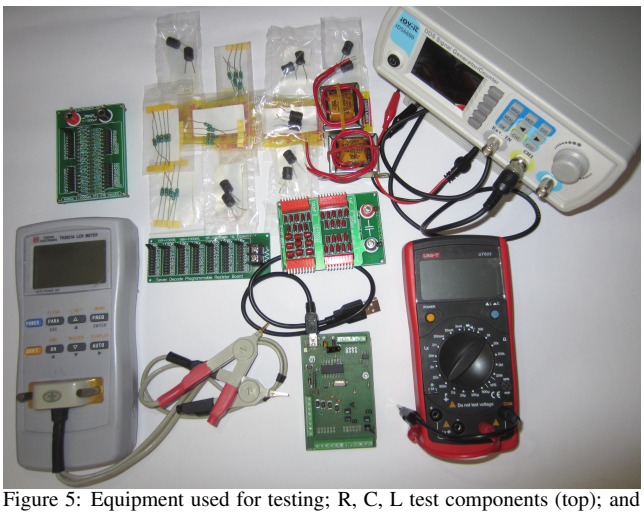

Figure 5: Equipment used for testing; R, C, L test components (top); and the Multiple-Sensor Interface (center bottom).

records (in 2 column tables) of the measured values of inductance, resistance, capacitance paired with measured frequency on the Multiple Sensor Interface device. For these tests (Fig.5) were used arrays(PCBs) of inductors, resistors, capacitors that allow to obtain various different values just by changing a jumper/switch, also were used single components (including in series or parallel association); these fixed value components were connected as the sensor on the device. The various figures with plots/graphs in this article will show both the experimental data obtained from the mentioned tests, as well the theoretical graphs obtained from circuit analysis of the device, for comparison purposes.

The experimental data of the mentioned tests is on: Appendix A (Tab. 2, Tab. 3, Tab. 1) is the $C_{sensor}(f)$, $L_{sensor}(f)$, $R_{sensor}(f)$ tables with C_1, C_2 as 2.2nF(JP on) or 21.8pF(JP off); Appendix B (Tab. 5 , Tab. 6 , Tab. 4) is the $R_{sensor}(f)$, $L_{sensor}(f)$, $C_{sensor}(f)$ tables with C_1, C_2 as 93nF(JP on) or 21.8pF(JP off); Appendix C (Tab. 7) is the $Illum(f)$ table with C_1=C_2=2.2nF(JP on) of a LDR sensor; Appendix E (Tab. 8) is the $h_{water}(f)$ table with C_1=C_2=2.2nF(JP on) of a water level sensor.

3.2 Sensor Interface Circuit Analysis

3.2.1 Multiple-Sensor Interface for inductive sensors

When is connected an inductor or inductive sensor the Multiple-Sensor Interface (Fig.2) may work as a Pierce oscillator(where the sensor is connected instead of a quartz crystal). The theoretical analysis for this type of oscillator, can be based on a model of 2 circuit blocks named 'A' and 'β' connected for feedback by connecting the output of one to the input other. The 'A' is an electronic amplifier providing voltage gain, the 'β' is an electronic filter providing frequency selection (resonance), so whatever voltage signal amplified by 'A' is frequency selected by 'β' and feed back to the input of A for further amplification. As known, this oscillator is start-up by whatever noise (v_s) available at the input of 'A', Fig.6 is a diagram depicting this concept.

With this type of oscillator, for determining the frequency of oscillation, may be used the Barkhausen stability criterion that says $A\beta = 1$ to be possible to occur sustained oscillations (oscillations on steady state analysis); where A and β represent the transfer function of the correspondingly named block.

The circuit analysis of the Pierce oscillator is available on

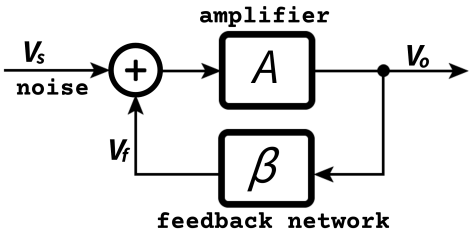

Figure 6: Diagram of model for the oscillator with an inductive sensor working as Pierce oscillator (model of feedback linear oscillator).

various text book (and also class notes); references about Pierce oscillator circuit analysis that are the author preference for understating how the Multiple-Sensor Int. may work as Pierce oscillator, are: "Crystal Oscillators" of "Digital Electronics" class notes by Peter McLean [1] ; "Microelectronic Circuit Design (4th ed.)" by R.C. Jaeger, T.N. Blalock [2] ; "Microelectronic Circuits (8th i. ed.)" by A. S. Sedra, K. C. Smith, T. C. Carusone, V. Gaudet [3] .

About the circuit analysis of the Pierce oscillator (and in generally with Colpitts type oscillators), a relevant conclusion is that the feedback network (block β) composed of 3 electrical components, that include the capacitors C_1 and C_2, must have an inductive part on the remaining (3rd) electrical component (for example: the piezoelectric crystal of a typical Pierce oscillator, or simply an inductor, or an inductive sensor, etc...), to be able to satisfy $A\beta = 1$ and so have oscillations on steady state analysis.

For the Pierce oscillator the equation that relates the oscillation frequency with the inductance and capacitance is a typical equation of LC oscillator circuits, using the definition of a "load capacitance" C_L as $(1/C_L) = (1/C_1) + (1/C_2)$.

The frequency of oscillation on the Pierce oscillator (using C_1, C_2, L_s) is:

$$\omega = \frac{1}{\sqrt{L_s C_L}} \quad \Leftrightarrow \quad f = \frac{1}{2\pi\sqrt{L_s C_L}} \tag{1}$$

So the expression (theoretical) of a value for inductance (L_s) as a function of frequency(f) is:

$$L_{sensor} = L_s = \frac{1}{4\pi^2 C_L f^2} = \frac{C_1 + C_2}{4\pi^2 C_1 C_2 f^2} \tag{2}$$

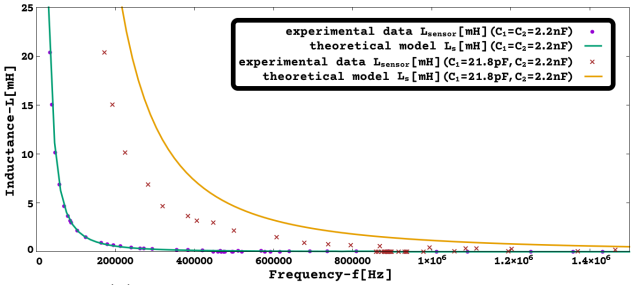

Figure 7: $L_s(f)$[mH]([Hz]) with C_1=C_2=2.2nF and C_1=21.78pF, C_2=2.2nF (Pierce osc., Multi-Sensor Int. with inductive sensor)

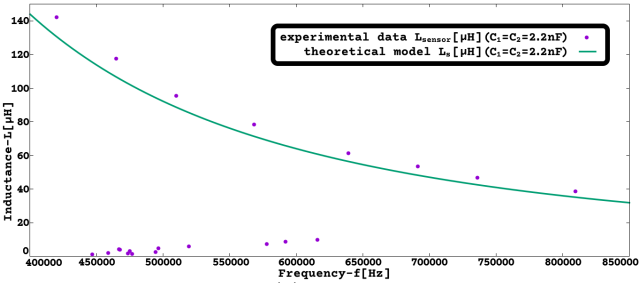

Figure 8: Frequency jump of $L_s(f)$[μH]([Hz]) with C_1=C_2=2.2nF (Pierce osc., Multi-Sensor Int. with inductive sensor).

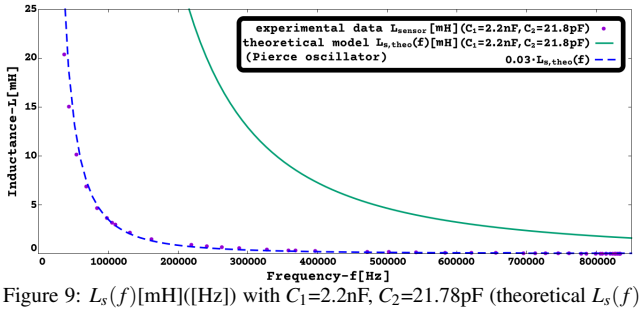

Figure 9: $L_s(f)$[mH]([Hz]) with C_1=2.2nF, C_2=21.78pF (theoretical $L_s(f)$ as a Pierce osc.).

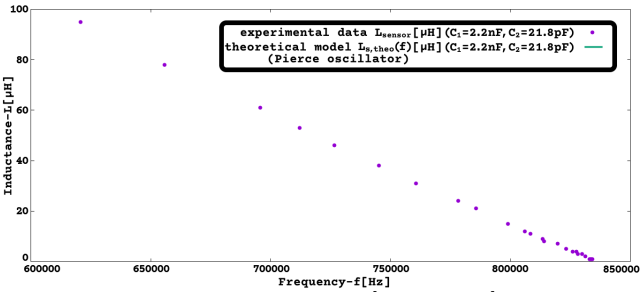

Figure 10: Experimental data of L_{sensor} in $[0\mu H; 100\mu H]$, with C_1=2.2nF, C_2=21.78pF (theoretical $L_s(f)$ as a Pierce osc. is out of plot range).

On experimental tests done was observed that when using C_1=C_2=2.2nF (JP.A and JP.B closed) or when using C_1=21.78pF (JP.A open), C_2=2.2nF (JP.B closed), with decreasing values of L_s connected, the oscillation frequency exhibited a sudden change, at some small value of L(around $10\mu H$ for C_1=C_2=2.2nF), not coherent with theoretical model of Pierce oscillator. This may be related to the fact that the same circuit also implements a Schmitt-trigger oscillator(next section), that oscillates under different criteria, so the author opinion is when L_s approaches some small value it may change from Pierce oscillator to Schmitt-trigger oscillator. Fig.7 and Fig.8 shows the experimental data for various inductance values connected as the sensor and the plot $L_s(f)$ using (2) with C_1=C_2=2.2nF and C_1=21.78pF, C_2=2.2nF.

Since the mentioned sudden change of oscillator mode and frequency is not adequate on a $L_s(f)$ function usable for sensor interfacing; then on experimental tests with jumper configuration: JP.A on and JP.B off (C_1=2.2nF, C_2=21.78pF), it was observed a continuous and progressive $f(L_{sensor})$ function. With C_1=2.2nF, C_2=21.78pF, the experimental L_{sensor} values followed a straight line for L_{sensor} in $[0\mu H; 100\mu H]$ (Fig.10), then for L_{sensor}>$100\mu H$ the experimental L_{sensor} has a shape with some visual similarity to theoretical (as Pierce oscillator), but with very different L_{sensor} values. Also apparently for larger values of L_{sensor} the theoretical (Pierce oscillator, JP.A on, JP.B off) $L_{s,theo}(f)$ could be approximated to the experimental data by a constant multiplicative factor ($L_{sensor} \approx 0.03 \cdot L_{s,theo}(f)$, for L_{sensor}>1mH), as visible in Fig.9.

For modeling(data fitting) purposes, the author knows that a function $L_s(f)$=$(a+(b/(c+d\cdot f)))\cdot(n\cdot f+m)$, where 'a,b,c,d,m,n' are constants to fit, can be fitted to experimental data on both low and high values of L_s.

On following section 3.3 was used an approximated model (for Schmitt-trigger oscillator) applied to Multiple-Sensor Interface with inductive sensor (JP.A on, JP.B off), that exhibited a theoretical $L_s(f)$ plot much closer to the experimental data, corroborating the hypothesis that with jumper configuration JP.A on, JP.B off (C_1=2.2nF, C_2=21.78pF), it operates as a Schmitt-trigger oscillator, where L_s acts as an impedance influencing C_1 charge and discharge speed.

On following section 3.4, also about inductive sensor (JP.A on, JP.B off), was used a theoretical model(for Schmitt-trigger oscillator) with some rude/obscene approximations; that model was successful in predicting the correct shape of $L_s(f)$ although with a somewhat considerable displacement to the experimental data.

3.2.2 *Multiple-Sensor Interface for resistive sensors*

In case of connecting a resistive sensor (or capacitive) to the Multiple-Sensor Interface it will not be able to satisfy the conditions for oscillation consequent of the Barkhausen criterion applied to the circuit as Pierce oscillator; so the conclusion is when a resistive sensor (or capacitive) is connected, it no longer is a Pierce oscillator. The Multiple-Sensor Interface is made using Schmitt-trigger inverters(high-speed Si-gate CMOS, 74HC14), and the hysteresis of the Schmitt-trigger can be used to implement another type of oscillator, the relaxation oscillator. So in the case of a resistive sensor the circuit to analyze is a Schmitt-trigger inverter connected to a network of resistors and capacitors.

To analyze this circuit the Schmitt-trigger inverter was replaced by a theoretical switch that changes the voltage of node v_o to V_{DDS} (power supply stabilized voltage for the sensor interface) when voltage v_i is lower than V_T^-, and changes v_o to GND when voltage v_i is higher than V_T^+.

So the circuit of Fig.11 is here analyzed to obtain $f(R_s)$, and then its inverse function $R_s(f)\approx R_{sensor}$ that may be useful for using/configuring the Multiple-Sensor Interface. Notice that $i_i\approx 0$ since v_i is the input of a Schmitt-trigger inverter (high-speed Si-gate CMOS) that has a very high input impedance and so $i_i\approx 0$ is an appropriate approximation simplifying the circuit. So from the circuit are obtained the equations: Nodes and loops: $i_4 = i_s + i_1$, $i_3 + i_s = i_2$, $i_o = i_3 + i_4$, $i_1 + i_2 = i_o$, $i_1 + i_2 = i_3 + i_4$, $v_1 - v_2 - v_s = 0$, $v_4 + v_s + v_2 - v_o = 0$, $v_4 + v_s - v_3 = 0$, $v_3 = v_o - v_2$, $v_4 = v_o - v_i$, $v_2 = v_i - v_s$.

Components: i_1=$C_1(dv_1/dt)$, i_2=$C_2(dv_2/dt)$, v_3=$R_2 i_3$, v_4=$R_1 i_4$, v_s=$R_s i_s$.

Solving:

$$\frac{v_o - v_i}{R_1} = \frac{v_s}{R_s} + C_1 \frac{dv_i}{dt} \tag{3}$$

$$\frac{v_o - v_i + v_s}{R_2} + \frac{v_s}{R_s} = C_2 \frac{dv_2}{dt} \tag{4}$$

Solving: $v_2 = v_i - v_s \Rightarrow dv_2/dt = d(v_i - v_s)/dt \Rightarrow dv_2/dt = (dv_i/dt) - (dv_s/dt)$

So using the previous result the (4) can be changed to:

$$\frac{v_o - v_i}{R_2} + \left(\frac{1}{R_2} + \frac{1}{R_s}\right) v_s = C_2 \left(\frac{dv_i}{dt} - \frac{dv_s}{dt}\right) \tag{5}$$

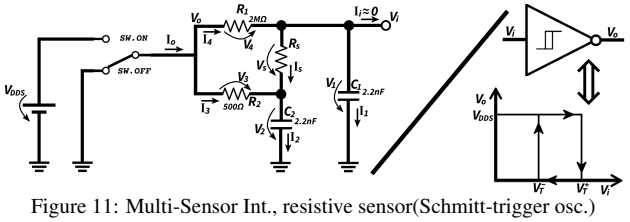

Figure 11: Multi-Sensor Int., resistive sensor(Schmitt-trigger osc.)

Solving (3) for v_s is obtained:

$$v_s = \frac{R_s(v_o - v_i)}{R_1} - R_s C_1 \frac{dv_i}{dt} \tag{6}$$

Calculating the derivative on both sides of (6) is obtained (remember v_o is a constant equal to V_{DDS} or GND depending on the position of the switch 'SW'):

$$\frac{dv_s}{dt} = \frac{-R_s}{R_1}\frac{dv_i}{dt} - R_s C_1 \frac{d^2 v_i}{dt^2} \tag{7}$$

Now using (6) and (7) to remove the variables v_s and dv_s/dt from equation (5) is obtained an equation solvable for determining $v_i(t)$:

$$\left(\frac{1}{R_2} + \frac{R_s}{R_2 R_1} + \frac{1}{R_1}\right)(v_o - v_i) = \left(C_1\left(1 + \frac{R_s}{R_2}\right) + C_2\left(1 + \frac{R_s}{R_1}\right)\right)\frac{dv_i}{dt} + R_s C_1 C_2 \frac{d^2 v_i}{dt^2} \tag{8}$$

The equation (8) is of the type: $c(v_o - v_i) = b(dv_i/dt) + a(d^2 v_i/dt^2)$ that has the general solution: $v_i(t) = v_o + k_1 e^{\lambda_1 t} + k_2 e^{\lambda_2 t}$, where k_1,k_2 are integration constants to be defined by 'initial conditions' and λ_1, λ_2 are defined by: $a\lambda^2 + b\lambda + c = 0 \Leftrightarrow \lambda = \frac{-b \pm \sqrt{b^2 - 4ac}}{2a}$ and e is the Euler-Napier constant $e = \sum_{n=0}^{\infty}(1/(n!))$.

So defining here a_r, b_r, c_r as the values of a, b, c for obtaining $v_i(t)$ when using a resistive sensor, as:

$a_r = R_s C_1 C_2$,

$b_r = (C_1(1 + (R_s/R_2))) + (C_2(1 + (R_s/R_1)))$,

$c_r = (1/R_2) + (R_s/(R_2 R_1)) + (1/R_1)$.

In order to obtain $v_i(t)$ for this circuit is required to calculate k_1 and k_2, that are constants to be defined by 'initial conditions', the value of these constants is related to the voltage (or electrical charge) on capacitors C_1 and C_2 at the moment the inverter gate changes its output voltage (high to low, or low to high), on the model used for analyzing the circuit that is when the 'theoretical switch' v_o changes state. Also, is only known the value of v_i (to be V_T^- or V_T^+) when the inverter gate v_o changes value, so is very difficult to calculate both k_1 and k_2 by algebraic manipulation. Admitting that $R_1 \gg R_2$ and that $C_1 \geqslant C_2$ (that is the case of the circuit that was studied and tested where R_1=2$M\Omega$ and R_2=500Ω), then is known that the capacitor C_2 will charge faster than C_1 for all values of R_s, and in case R_s has an impedance comparable to R_2 then C_2 will charge much faster than C_1. So the voltage (and electrical charge) of C_2 follows closely the values of v_o and so will be of small relevance to the initial conditions of the circuit, thus $v_i(t) = v_o + k_1 e^{\lambda_1 t} + k_2 e^{\lambda_2 t}$ can be approximated as single exponential function $v_i(t) \approx v_o + k e^{\lambda t}$, this approximation is implied on the following calculations.

Is selected the solution $\lambda_2 = \frac{-b + \sqrt{b^2 - 4ac}}{2a}$ by setting k_1=0, because is the one that provides an adequate value for $v_i(t)$, $f(R_s)$, consistent with experimental data, however for obtaining the (approximate) function $R_s(f)$ any may be used.

For convenience of a $v_i(t)$ more similar to typical RC circuits is defined $\tau = -1/\lambda$, and so $v_i(t) = v_o + k_2 e^{-t/\tau_2}$ (or more appropriately: $v_i(t) \approx v_o + k_2 e^{-t/\tau_2}$).

Charging time of C_1: $v_o = V_{DDS}$

$v_i(t{=}0){=}V_T^- \rightarrow V_T^- = V_{DDS} + k_2 e^0 \rightarrow k_2 = V_T^- - V_{DDS}$

$v_i(t{=}T_C){=}V_T^+ \rightarrow V_T^+ = V_{DDS} + k_2 e^{-T_C/\tau_2} \rightarrow$

$\rightarrow \quad T_C = -\tau_2 ln((V_T^+ - V_{DDS})/(V_T^- - V_{DDS}))$

Discharging time of C_1: $v_o = 0$

$v_i(t{=}0){=}V_T^+ \rightarrow V_T^+ = 0 + k_2 e^0 \quad \rightarrow \quad k_2 = V_T^+$

$v_i(t{=}T_D){=}V_T^- \rightarrow V_T^- = 0 + k_2 e^{-T_D/\tau_2} \rightarrow$

$\rightarrow \quad T_D = -\tau_2 ln(V_T^-/V_T^+)$

The time for a complete cycle of charge and discharge of C_1 is: $T = T_C + T_D$; the frequency of $v_i(t)$ is $f = 1/T$.

Solving: $T = -\tau_2\left(ln\left(\frac{V_T^+ - V_{DDS}}{V_T^- - V_{DDS}}\right) + ln\left(\frac{V_T^-}{V_T^+}\right)\right) \Leftrightarrow$

$T = \tau_2 ln\left(\frac{(V_T^- - V_{DDS})V_T^+}{(V_T^+ - V_{DDS})V_T^-}\right)$

For convenience defining the constant 'H' by:

$$H = ln\left(\frac{(V_T^- - V_{DDS})V_T^+}{(V_T^+ - V_{DDS})V_T^-}\right),$$

then $f = 1/T \Leftrightarrow f = 1/(\tau_2 H) \Leftrightarrow f = -\lambda_2/H$.

So the expression (theoretical) of an approximate value for resistance (R_s) as a function of frequency(f) is:

$$R_{sensor} \approx R_s = \frac{(C_1 + C_2)R_2 R_1 H f - R_2 - R_1}{(C_2 R_2 H f - 1)(C_1 R_1 H f - 1)} \tag{9}$$

Using the values C_1=C_2=2.2nF, R_2=500Ω, R_1=2$M\Omega$, V_T^-=1.2V, V_T^+=2.2V, V_{DDS}=4.18V, is obtained H=1.01496, Fig.12 shows experimental data for Multiple-Sensor Interface with various resistance values connected as the sensor and also shows $R_s(f)$ using (9) with the mentioned values of C_1, C_2, R_2, R_1, H.

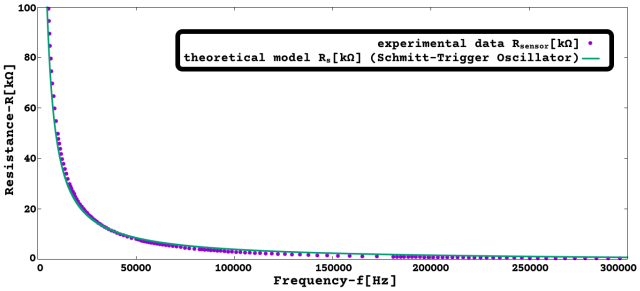

Figure 12: $R_s(f)$ [kΩ], frequency in [0Hz, 300kHz] (Schmitt-trigger oscillator, Multiple-Sensor Interface with resistive sensor).

3.2.3 *Multiple-Sensor Interface for capacitive sensors*

In case of connecting a capacitive sensor (or resistive) to the Multiple-Sensor Interface it will not be able to satisfy the conditions for oscillation consequent of the Barkhausen criterion applied to the circuit as Pierce oscillator; and so it is again a Schmitt-trigger relaxation oscillator. To analyze this circuit the Schmitt-trigger inverter was replaced by a theoretical switch (Schmitt-trigger), just like previously with resistive sensors.

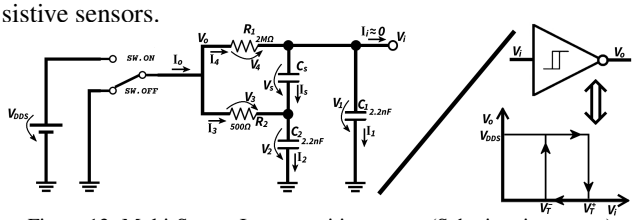

Figure 13: Multi-Sensor Int., capacitive sensor (Schmitt-trigger osc.)

So the circuit of Fig.13 is here analyzed to obtain $f(C_s)$, and then its inverse function $C_s(f) \approx C_{sensor}$ that is useful for using/configuring the Multiple-Sensor Interface. Notice that $i_i \approx 0$ since v_i is the input of the Schmitt-trigger inverter(high-

speed Si-gate CMOS) that has a very high input impedance and so $i_i \approx 0$ is an appropriate approximation simplifying the circuit. So from the circuit are obtained the equations:

Nodes and loops: $i_4 = i_s + i_1$, $i_3 + i_s = i_2$, $i_o = i_3 + i_4$, $i_1 + i_2 = i_o$, $i_1 + i_2 = i_3 + i_4$, $v_1 - v_2 - v_s = 0$, $v_4 + v_s + v_2 - v_o = 0$, $v_4 + v_s - v_3 = 0$, $v_3 = v_o - v_2$, $v_4 = v_o - v_i$, $v_2 = v_i - v_s$.

Components: $i_1 = C_1(dv_1/dt)$, $i_2 = C_2(dv_2/dt)$, $v_3 = R_2 i_3$, $v_4 = R_1 i_4$, $i_s = C_s(dv_s/dt)$.

Solving:

$$\frac{v_o - v_i}{R_1} = C_s \frac{dv_s}{dt} + C_1 \frac{dv_i}{dt} \tag{10}$$

$$\frac{v_o - v_2}{R_2} + C_s \frac{dv_s}{dt} = C_2 \frac{dv_2}{dt} \tag{11}$$

$$\frac{v_o - v_2}{R_2} + \frac{v_o - v_i}{R_1} = C_1 \frac{dv_i}{dt} + C_2 \frac{dv_2}{dt} \tag{12}$$

Since $v_s = v_i - v_2$ then $dv_s/dt = (dv_i/dt) - (dv_2/dt)$, and so using it on equation (10), is obtained:

$$\frac{dv_2}{dt} = \left(1 + \frac{C_1}{C_s}\right) \frac{dv_i}{dt} - \frac{v_o - v_i}{C_s R_1} \tag{13}$$

Using $dv_s/dt = (dv_i/dt) - (dv_2/dt)$ and (13) on equation (11), is obtained:

$$v_2 = v_o + \frac{R_2(C_2+C_s)(v_o - v_i)}{C_s R_1} + R_2 C_s \left(1 - \left(1 + \frac{C_2}{C_s}\right)\left(1 + \frac{C_1}{C_s}\right)\right) \frac{dv_i}{dt} \tag{14}$$

Calculating the derivative of (14) is obtained:

$$\frac{d(v_2)}{dt} = -\frac{R_2(C_2+C_s)}{C_s R_1} \frac{dv_i}{dt} + R_2 C_s \left(1 - \left(1 + \frac{C_2}{C_s}\right)\left(1 + \frac{C_1}{C_s}\right)\right) \frac{d^2 v_i}{dt^2} \tag{15}$$

Now using (14) and (15) to remove the variables v_2 and dv_2/dt from the equation (12), is obtained an equation solvable for determining $v_i(t)$:

$$v_o - v_i = (R_2(C_2+C_s) + R_1(C_1+C_s)) \frac{dv_i}{dt} + R_2 R_1 (C_1 C_2 + C_s(C_1+C_2)) \frac{d^2 v_i}{dt^2} \tag{16}$$

The equation (16) is of the type: $c(v_o - v_i) = b(dv_i/dt) + a(d^2 v_i/dt^2)$, that has the general solution:
$v_i(t) = v_o + k_1 e^{\lambda_1 t} + k_2 e^{\lambda_2 t}$, where k_1,k_2 are integration constants to be defined by 'initial conditions' and λ_1, λ_2 are defined by: $a\lambda^2 + b\lambda + c = 0 \Leftrightarrow \lambda = \frac{-b \pm \sqrt{b^2 - 4ac}}{2a}$ and e is the Euler-Napier constant $e = \sum_{n=0}^{\infty} (1/(n!))$.

So defining here a_c, b_c, c_c as the values of a, b, c for obtaining $v_i(t)$ when using a capacitive sensor, as: $c_c = 1$,
$b_c = (R_2(C_2 + C_s) + R_1(C_1 + C_s))$,
$a_c = R_2 R_1 (C_1 C_2 + C_s(C_1 + C_2))$.

In order to obtain $v_i(t)$ for this circuit is required to calculate k_1 and k_2, to be defined by 'initial conditions'; notice that this circuit has 3 capacitors that store electrical charge defining 'initial conditions', but the location of C_s connected between C_1 and C_2 implies that the voltage of C_s (or its electrical charge) is completely defined/known by the voltages (or electrical charges) on C_1 and C_2.

Here are made the same approximation/simplification of $v_i(t) \approx v_o + k e^{\lambda t}$, as explained and done on the case of resistive sensor.

Is selected the solution $\lambda_2 = \frac{-b + \sqrt{b^2 - 4ac}}{2a}$ by setting $k_1 = 0$, because is the one that provides an adequate value for $v_i(t)$, $f(C_s)$, consistent with experimental data, however for obtaining the function $C_s(f)$ any may be used.

For convenience of a $v_i(t)$ more similar to typical RC circuits is defined $\tau = -1/\lambda$, and so $v_i(t) = v_o + k_2 e^{-t/\tau_2}$ (or more appropriately: $v_i(t) \approx v_o + k_2 e^{-t/\tau_2}$).

So when is connected a capacitive sensor (C_s) the differential equation and solution $v_i(t)$ are the same as when is connected a resistive sensor (R_s), the only differences are in the values of a, b, c; and as such the equations of f(frequency) and T(period) are also the same and are reused from the previous section.

The constant 'H' defined by:

$$H = ln\left(\frac{(V_T^- - V_{DDS})V_T^+}{(V_T^+ - V_{DDS})V_T^-}\right),$$

and $f = 1/T \Leftrightarrow f = 1/(\tau_2 H) \Leftrightarrow f = -\lambda_2/H$.

So the expression (theoretical) of an approximate value for capacitance (C_s) as a function of frequency(f) is:

$$C_{sensor} \approx C_s = \frac{(C_1 R_1 + C_2 R_2) H f - 1 - C_1 C_2 R_1 R_2 H^2 f^2}{H f((C_1 + C_2) R_1 R_2 H f - R_1 - R_2)} \tag{17}$$

Using the values C_1=C_2=2.2nF, R_2=500Ω, R_1=2MΩ, V_T^-=1.2V, V_T^+=2.2V, V_{DDS}=4.18V, is obtained H=1.01496, Fig.14 shows the plot of $C_s(f)$ using (17) with the mentioned values of C_1, C_2, R_2, R_1, H.

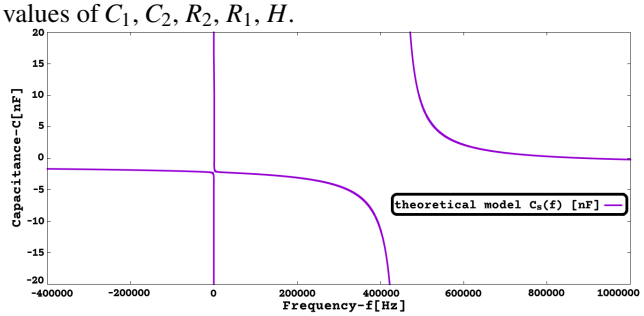

Figure 14: $C_s(f)$ [nF], frequency in [-400kHz, 1MHz] (Schmitt-trigger oscillator, Multiple-Sensor Interface with capacitive sensor).

Analyzing the plot in Fig.14 by firstly looking at plot regions with C_s>0, its visible that the $C_s(f)$ plot is close to being over the vertical axis (f=0) and this would mean that for all values of C_s the frequency would be close to zero ($f \approx 0$), but visible to the right is another curve that is also placed on the area of C_s>0 (for frequency [447957Hz, 895689Hz]) and at a first view this curve would seem appropriate. But strangely on C_s>0, f>0 for each value of C_s are 2 values of frequency, while for C_s<0, f>0 each value of C_s has only one possible value of frequency (f<0 is considered meaningless/ignored).

The experimental data shows that the way the oscillator works using a capacitive sensor is different from what some would expect on a first view of the plot $C_s(f)$, in order to compare the experimental data with the theoretical model is shown in Fig.15 and Fig.16 the experimental data for Multiple-Sensor Interface with various capacitance values connected as the sensor and also the plot of $abs(C_s(f))$ $(= |C_s(f)|)$ using (17) with the mentioned values of C_1, C_2, R_1, R_2, H. So it seems that the obtained function of $C_s(f)$ although strangely indicates negative values for the sensor capacitance it can provide a theoretical curve/plot similar to what was obtained on the experimental data for C_{sensor}. On the following sections is given a better insight on why $C_s(f)$ has a negative value.

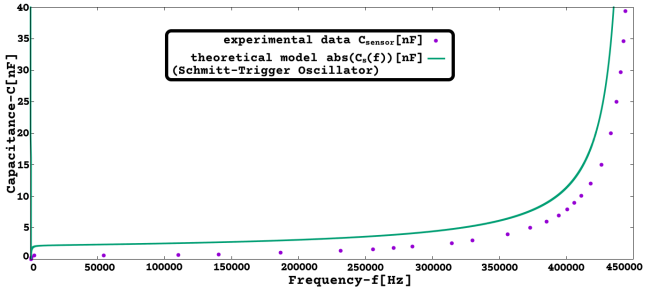

Figure 15: $|C_s(f)|$ [nF], frequency in [0Hz, 450kHz] (Schmitt-trigger osc., Multi-Sensor with capacitive sensor)

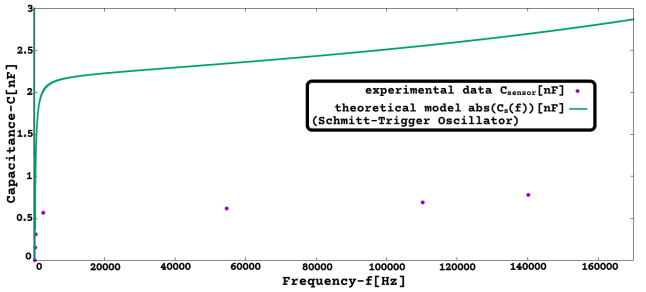

Figure 16: $|C_s(f)|$ [nF], frequency in [0Hz, 170kHz] (Schmitt-trigger osc., Multi-Sensor with capacitive sensor)

3.2.4 Multiple-Sensor Int. for measuring frequency

For measuring frequency of an external voltage signal (between 0V and V_{DDS}, so preferentially a digital signal or in case of analog signal it should be limited/trimmed before) is possible to use the mentioned Multiple-Sensor Interface and so using the same port/connector of the device. For this the user should remove/open the jumpers "JP.A", "JP.B" making the capacitors C1-A, C2-B active on the circuit, this will make $C_1 = C_2 = 21.8pF$ that is a quite low capacitance that will have an insignificant effect on the external voltage signal. The external voltage signal should be connected to the 1st pin of the sensor channel that is the one connected directly to the input of the Schmitt-trigger inverter, so that the inverter is directly driven by the external voltage signal, then the Multiple-Sensor Interface is just a converter of the voltage signal to a square wave signal where its frequency will be measured through the counter/timer of the PIC18F2550.

The external voltage signal would preferentially be from a sensor with a square wave output, and the sensor have its power supplied by one of the V_{DDS},GND ports/connectors of the sensor interface device or by an external connection to the same power supply used to power the device.

3.3 Alternative Approximate Circuit Analysis

3.3.1 Sensor interface circuit simplified

The Multiple-Sensor Interface circuit when working as Schmitt-trigger oscillator (using R_s, C_s, or L_s with specific C_1,C_2 values) can be studied and understood in a more intuitive way by making some simplification/approximation that may be inaccurate for quantitative purposes but still captures its essence, with the benefit of exposing how it works and resulting in much simpler differential equations. So the interface circuit is a more complex Schmitt-trigger oscillator, but its essence is the same, it is just some capacitors being charged by currents that pass through some resistors, and the voltage on a capacitor(v_i) will trigger(at V_T^- or V_T^+) a switch(electronic inverter) to change the voltage(v_o) [4] .

So the sensor and interface circuit can be described approximately as a basic Schmitt-trigger oscillator that only has one capacitor and one resistor (that determine the frequency of oscillation), and so was used the simplified circuit in Fig.17 where C_{approx} is a capacitor and R_{approx} is a resistor that approximate in overall the capacitance and resistance of the sensor interface oscillator.

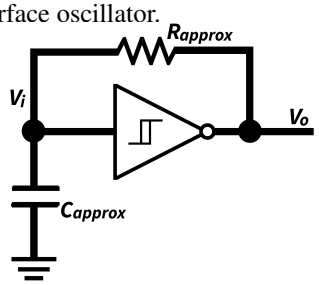

Figure 17: Schematic of a basic Schmitt-trigger oscillator to be used as an approximation of the circuit of Multiple-Sensor Interface

To build expressions of C_{approx} and R_{approx} that include R_1, R_2, C_1, C_2 are considered initially 2 extreme cases of the sensor impedance(Z_s): 1st $|Z_s|$=0 the sensor can be replaced by a wire, and 2nd $|Z_s|$=∞ the sensor can be removed(open circuit), these 2 extreme cases possible for the sensor impedance are represented in Fig.18 .

Now the sensor can be described as an electric connection that can be weakened or intensified depending on the sensor impedance, so when $|Z_s|$ changes progressively from 0 to $+\infty$ the circuit behavior changes progressively and smoothly from the behavior of the left circuit to the behavior of right circuit of Fig.18. So to obtain equations for R_{approx} and C_{approx} was selected an expression that allows to change smoothly the resistance and capacitance of the left side circuit to the resistance and capacitance of the right side circuit of Fig.18.

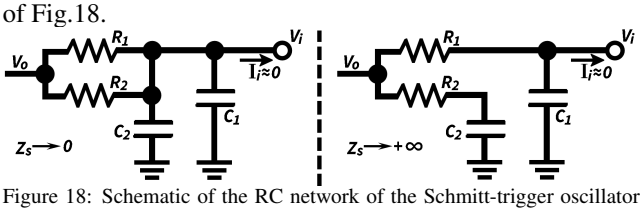

Figure 18: Schematic of the RC network of the Schmitt-trigger oscillator for the 2 extreme cases of sensor impedance (Z_s).

So as in Fig.18, here are the values of C_{approx} and R_{approx} for the 2 extreme values of $|Z_s|$=0 and $|Z_s|$=+∞:

$C_{approx}(Z_s$=0)=C_1+C_2; $C_{approx}(Z_s$=∞)=C_1;

$R_{approx}(Z_s$=0)=$(R_1R_2)/(R_1$+$R_2)$; $R_{approx}(Z_s$=∞)=R_1;

3.3.2 R_{approx} and C_{approx} for a resisitve sensor (R_s)

Here are functions modeled to describe C_{approx} and R_{approx} (with resistive sensor) with a smooth transition from its values at $|Z_s|$=0 and $|Z_s|$=$+\infty$, where $|Z_s|$=R_s:

$$C_{approx} = (C_1 + C_2)\frac{R_1}{|Z_s| + R_1} + C_1\frac{|Z_s|}{|Z_s| + R_1} \tag{18}$$

$$R_{approx} = \frac{R_1R_2}{(R_1 + R_2)}\frac{2R_1}{(|Z_s| + 2R_1)} + R_1\frac{|Z_s|}{|Z_s| + 2R_1} \tag{19}$$

Using the equations: f=$1/T \Leftrightarrow f$=$1/(\tau H) \Leftrightarrow f$=-$\lambda/H$, and using τ=$R_{approx}C_{approx}$, where $|Z_s|$ was removed using $|Z_s|$=R_s, it can be obtained $R_s(f)$.

Using values V_T^-=1.2V, V_T^+=2.2V, V_{DDS}=4.18V, is obtained H=1.01496 (valid for any type of sensor).

Using the values C_1=C_2=2.2nF, R_2=500Ω, R_1=2$M\Omega$, H=1.01496 with the approximate model (C_{approx}, R_{approx}), is obtained the plot of $R_s(f)$ in Fig.19.

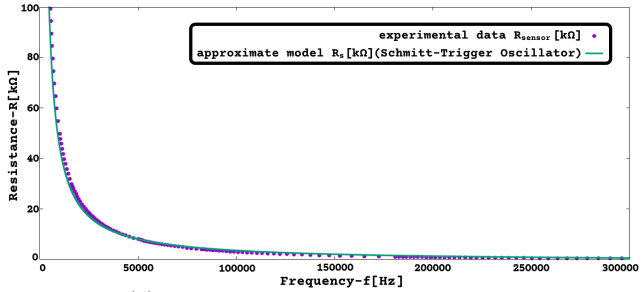

Figure 19: $R_s(f)$ [kΩ] by approximate model (C_{approx}, R_{approx}; Multi-Sensor Int. with resistive sensor).

3.3.3 R_{approx} and C_{approx} for an inductive sensor (L_s)

This approximate model for the interface circuit with inductive sensor is only valid for jumper configuration(capacitor values) that make it work as Schmitt-trigger oscillator, as is expected for JP.A closed, JP.B open (C_1=2.2nF, C_2=21.78pF). Here are functions modeled to describe C_{approx} and R_{approx} (with inductive sensor) with a smooth transition from its values at $|Z_s|$=0 and $|Z_s|=+\infty$, where $|Z_s|=2\pi f L_s$:

$$C_{approx} = (C_1 + C_2)\frac{R_1}{|Z_s| + R_1} + C_1\frac{|Z_s|}{|Z_s| + R_1} \tag{20}$$

$$R_{approx} = \frac{R_1 R_2}{(R_1 + R_2)}\frac{R_1}{(|Z_s| + R_1)} + R_1\frac{|Z_s|}{|Z_s| + R_1} \tag{21}$$

Using the values C_1=2.2nF, C_2=21.78pF, R_2=500Ω, R_1=2MΩ, H=1.01496 with the approximate model (C_{approx}, R_{approx}), is obtained the plot of $L_s(f)$ in Fig.20 and Fig.21.

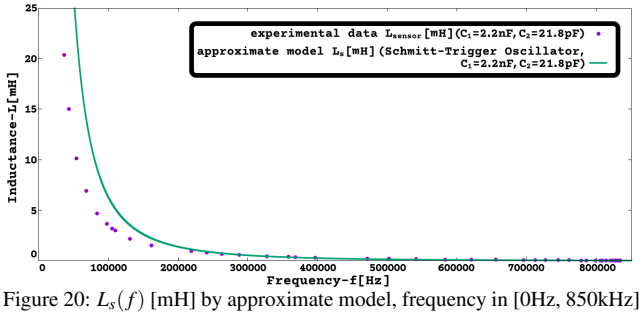

Figure 20: $L_s(f)$ [mH] by approximate model, frequency in [0Hz, 850kHz] (C_{approx}, R_{approx}; Multi-Sensor Int. with inductive sensor)

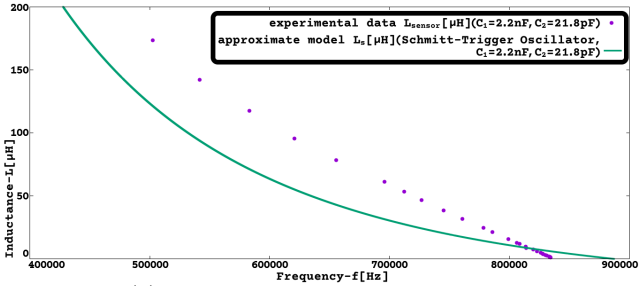

Figure 21: $L_s(f)$ [μH] by approximate model, frequency in [400kHz, 900kHz] (C_{approx}, R_{approx}; Multi-Sensor Int. with inductive sensor)

3.3.4 R_{approx} and C_{approx} for a capacitive sensor (C_s)

Here are functions modeled to describe C_{approx} and R_{approx} (with capacitive sensor) with a smooth transition from its values at $|Z_s|$=0 and $|Z_s|=+\infty$, where $|Z_s|=1/(2\pi f C_s)$:

$$C_{approx} = (C_1 + C_2)\frac{R_1}{|Z_s| + R_1} + C_1\frac{|Z_s|}{|Z_s| + R_1} \tag{22}$$

$$R_{approx} = \frac{R_1 R_2}{(R_1 + R_2)}\frac{R_1}{(|Z_s| + R_1)} + R_1\frac{|Z_s|}{|Z_s| + R_1} \tag{23}$$

Using the values C_1=C_2=2.2nF, R_2=500Ω, R_1=2MΩ, H=1.01496, with the approximate model (C_{approx}, R_{approx}), is obtained the plot $C_s(f)$ in Fig.22 and Fig.23.

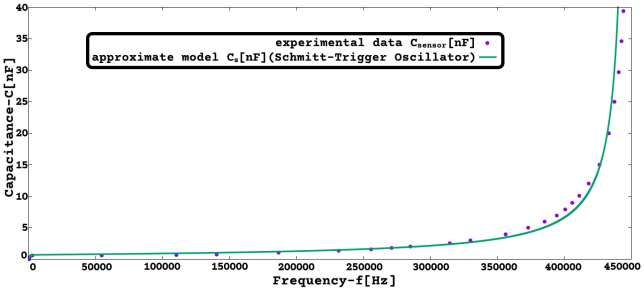

Figure 22: $C_s(f)$ [nF] by approximate model, frequency in [0Hz, 450kHz] (C_{approx}, R_{approx}; Multi-Sensor Int. with capacitive sensor)

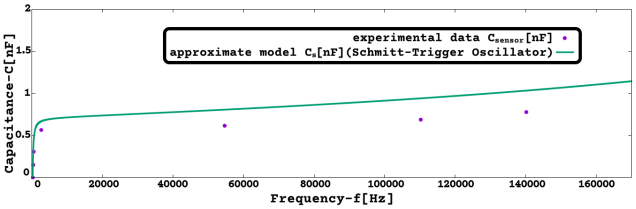

Figure 23: $C_s(f)$ [nF] by approximate model, frequency in [0Hz, 170kHz] (C_{approx}, R_{approx}; Multi-Sensor Int. with capacitive sensor)

3.4 *Multiple-Sensor Interface for inductive sensors as Schmitt-trigger oscillator*

Also is possible a theoretical analysis of the Multiple-Sensor Interface with an inductive sensor working continuously as a Schmitt-trigger oscillator observed when jumper configuration is JP.A on, JP.B off (C_1=2.2nF, C_2=21.78pF), although some approximations were required to be able to obtain a $L_s(f)$ function.

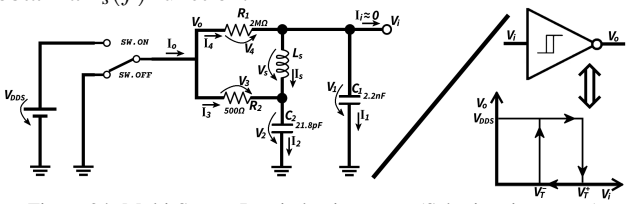

Figure 24: Multi-Sensor Int., inductive sensor(Schmitt-trigger osc.)

So the circuit of Fig.24 is here analyzed to obtain an approximation of $f(L_s)$, and of its inverse function $L_s(f)\approx L_{sensor}$ that is useful for using/configuring the Multiple-Sensor Interface. Notice that $i_i\approx 0$ since v_i is the input of the Schmitt-trigger inverter(high-speed Si-gate CMOS) that has a very high input impedance and so $i_i\approx 0$ is an appropriate approximation simplifying the circuit. So from the circuit are obtained the equations:

Nodes and loops: $i_4 = i_s + i_1$, $i_3 + i_s = i_2$, $i_o = i_3 + i_4$, $i_1 + i_2 = i_o$, $i_1 + i_2 = i_3 + i_4$, $v_1 - v_2 - v_s = 0$, $v_4 + v_s + v_2 - v_o = 0$, $v_4 + v_s - v_3 = 0$, $v_3 = v_o - v_2$, $v_4 = v_o - v_i$, $v_2 = v_i - v_s$.

Components: i_1=$C_1(dv_1/dt)$, i_2=$C_2(dv_2/dt)$, v_3=$R_2 i_3$, v_4=$R_1 i_4$, v_s=$L_s(di_s/dt)$.

Solving:

$$\frac{v_o - v_2}{R_2} + \frac{v_o - v_i}{R_1} = C_1\frac{dv_i}{dt} + C_2\frac{dv_2}{dt} \tag{24}$$

$$v_2 = v_i - L_s\frac{di_s}{dt} \tag{25}$$

$$\frac{v_o - v_i}{R_1} = i_s + C_1\frac{dv_i}{dt} \tag{26}$$

From (25) is obtained $dv_2/dt = (dv_i/dt) - L_s(d^2i_s/dt^2)$, and so using it on equation (24), is obtained:

$$(v_o - v_i)\left(\frac{1}{R_1}+\frac{1}{R_2}\right)+\frac{L_s}{R_2}\frac{di_s}{dt} = (C_1+C_2)\frac{dv_i}{dt} - L_sC_2\frac{d^2i_s}{dt^2} \quad (27)$$

From equation (26) is obtained:

$$i_s = \frac{v_o - v_i}{R_1} - C_1\frac{dv_i}{dt} \quad \Rightarrow \quad \frac{di_s}{dt} = -\frac{1}{R_1}\frac{dv_i}{dt} - C_1\frac{d^2v_i}{dt^2}$$
$$\Rightarrow \quad \frac{d^2i_s}{dt^2} = -\frac{1}{R_1}\frac{d^2v_i}{dt^2} - C_1\frac{d^3v_i}{dt^3} \quad (28)$$

Using (28), i_s can be eliminated from eq. (27), obtaining:

$$\left(\frac{1}{R_1}+\frac{1}{R_2}\right)(v_o - v_i) =$$
$$\left(C_1+C_2+\frac{L_s}{R_1R_2}\right)\frac{dv_i}{dt} + L_s\left(\frac{C_1}{R_2}+\frac{C_2}{R_1}\right)\frac{d^2v_i}{dt^2} + L_sC_1C_2\frac{d^3v_i}{dt^3} \quad (29)$$

The equation (29) is of the type: $d(v_o - v_i) = c(dv_i/dt) + b(d^2v_i/dt^2) + a(d^3v_i/dt^3)$ that has the general solution: $v_i(t) = v_o + k_1e^{\lambda_1 t} + k_2e^{\lambda_2 t} + k_3e^{\lambda_3 t}$, where k_1,k_2, k_3 are integration constants to be defined by 'initial conditions' and λ_1, λ_2, λ_3 are defined by: $a\lambda^3 + b\lambda^2 + c\lambda + d = 0$ and e is the Euler-Napier constant $e = \sum_{n=0}^{\infty}(1/(n!))$.

So defining here a_l, b_l, c_l, d_l as the values of a, b, c, d for obtaining $v_i(t)$ when using an inductive sensor, as:

$a_l = L_sC_1C_2$, $\quad b_l = L_s((C_1/R_2)+(C_2/R_1))$,

$c_l = C_1+C_2+(L_s/(R_1R_2))$, $\quad d_l = (1/R_1)+(1/R_2)$.

In order to obtain $v_i(t)$ for this circuit is required to calculate k_1, k_2 and k_3, that are constants to be defined by 'initial conditions', the value of these constants is related to the voltage (or electrical charge) on capacitors C_1 and C_2, and also to the electric current on the inductive sensor, at the moment the inverter gate changes its output voltage (high to low, or low to high), on the model used for analyzing the circuit that is when the 'theoretical switch' v_o changes state. Also, is only known the value of v_i (to be V_T^- or V_T^+) when the inverter gate v_o changes value, so is very difficult to calculate k_1, k_2, k_3 by algebraic manipulation. Admitting that $R_1 \gg R_2$ and that $C_1 \geqslant C_2$ (that is the case of the circuit that was studied and tested where R_1=2$M\Omega$ and R_2=500Ω), then is known that the capacitor C_2 will charge faster than C_1 for all values of Z_s (determined by the value L_s), and in case Z_s has an impedance comparable to R_2 then C_2 will charge much faster than C_1. So the voltage (and electrical charge) of C_2 follows closely the values of v_o and so will be of small relevance to the initial conditions of the circuit.

The inclusion of an inductor (the inductive sensor) makes the behavior of this circuit more complex and so the appearance of a 3rd degree differential equation; so in order to obtain an expression for $L_s(f)$ in a similar way as previously for resistive and capacitive sensors, are made the following approximations: 1 - The determination of $L_s(f)$ will be made in two domains, one expression of $L_s(f)$ valid for high frequency and other expression of $L_s(f)$ for low and middle frequency of the operation of the Schmitt-trigger oscillator. The author observed that high frequency operation is dominated by the 1st-root of $a\lambda^3 + b\lambda^2 + c\lambda + d = 0$ that is a real number; and observed that low and middle frequency operation is dominated by the 2nd-root and 3rd-root of $a\lambda^3 + b\lambda^2 + c\lambda + d = 0$ that are imaginary numbers.

2 - Regarding the low and middle frequency operation that is dominated by the 2nd-root and 3rd-root of the 3rd degree equation, will be made a 'rude' approximation of $v_i(t) \approx v_o + k_{23}e^{\lambda_{23}t}$, where $k_{23} = k_2 + k_3$ and $\lambda_{23} = (\lambda_2 + \lambda_3)/2$. Also is relevant to note that by adding λ_2 with λ_3 will nullify the imaginary part resulting in a real number, and also that $\lambda_{23} = (\lambda_2 + \lambda_3)/2 = Re[\lambda_2] = Re[\lambda_3]$.

3 - Regarding the high frequency operation that is dominated by the 1st-root of the 3rd degree equation, will be made the approximation of $v_i(t) \approx v_o + k_1e^{\lambda_1 t}$.

The mentioned approximations resulting in $v_i(t) \approx v_o + ke^{\lambda t}$, allows the theoretical analysis already used for resistive and capacitive sensor to be reused again here, for obtaining an approximation of $L_s(f)$.

So for an inductive sensor, just like with resistive or capacitive sensor, is used the function $v_i(t) \approx v_o + ke^{-t/\tau}$, where $\tau = -1/\lambda$, and the constant 'H' defined by:

$$H = ln\left(\frac{(V_T^- - V_{DDS})V_T^+}{(V_T^+ - V_{DDS})V_T^-}\right),$$

and $f = 1/T \Leftrightarrow f = 1/(\tau H) \Leftrightarrow f = -\lambda/H$.

So applying the previously mentioned approximations is obtained: $f_{high} \approx -\lambda_1/H$; $\quad f_{low,middle} \approx -\lambda_{23}/H$.

So the expression (theoretical) of an approximate value for inductance ($L_{s,HF}$) as a function of frequency(f) for high frequency is:

$$L_{sensor,HF} \approx L_{s,HF} = \frac{R_1 + R_2 - (C_1+C_2)R_1R_2Hf}{Hf(C_1R_1Hf-1)(C_2R_2Hf-1)} \quad (30)$$

So the expression (theoretical) of an approximate value for inductance ($L_{s,LMF}$) as a function of frequency(f) for low and middle frequency is:

$$L_{sensor,LMF} \approx L_{s,LMF} = (C_1{}^2R_1{}^2R_2 + C_2{}^2R_2{}^2R_1$$
$$- 2R_1{}^2R_2{}^2Hf(C_1{}^2C_2 + C_2{}^2C_1))/(8C_1{}^2C_2{}^2R_1{}^2R_2{}^2H^3f^3$$
$$- 8C_1C_2{}^2R_1R_2{}^2H^2f^2 - 8C_1{}^2C_2R_1{}^2R_2H^2f^2 + 2C_2{}^2R_2{}^2Hf$$
$$+ 6C_1C_2R_1R_2Hf + 2C_1{}^2R_1{}^2Hf - C_1R_1 - C_2R_2) \quad (31)$$

Using the values C_1=2.2nF, C_2=21.78pF, R_2=500Ω, R_1=2$M\Omega$, V_T^-=1.2V, V_T^+=2.2V, V_{DDS}=4.18V, is obtained H=1.01496, Fig.25 shows the plot of $L_{s,HF}(f)$ using (30) with the mentioned values of C_1, C_2, R_2, R_1, H.

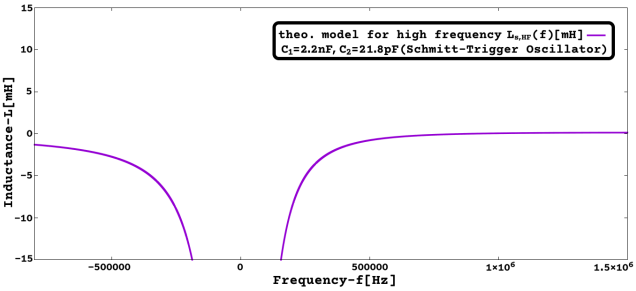

Figure 25: $L_{s,HF}(f)$ [mH], frequency in [-800kHz, 1.5MHz] (Sch-trig. osc., Multi-Sensor Int. with inductive sensor, HF approx. function).

Observing Fig.25 is noticeable that $L_{s,HF}(f)$ is almost always negative, except for frequency above around 900kHz. However drawing the plot of $abs(L_{s,HF}(f))$ ($= |L_{s,HF}(f)|$) along with experimental data for Multiple-Sensor Interface with various inductance values connected as the sensor (in Fig.26 and Fig.27), like was done before for the plots of a capacitive sensor, is then visible that the shape of $abs(L_{s,HF}(f))$ resembles the experimental data, however

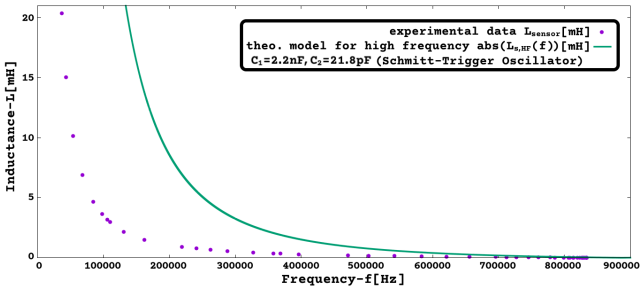

Figure 26: $abs(L_{s,HF}(f))$ [mH], frequency in [0Hz, 900kHz] (Sch-trig. osc., Multi-Sensor Int. with inductive sensor, HF approx. function).

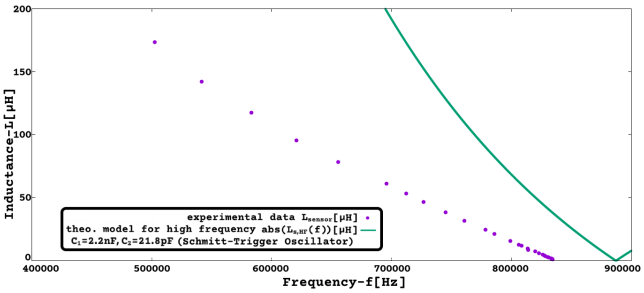

Figure 27: $abs(L_{s,HF}(f))$ [μH], frequency in [400kHz, 900kHz] (Sch-trig. osc., Multi-Sensor Int. with inductive sensor, HF approx. function).

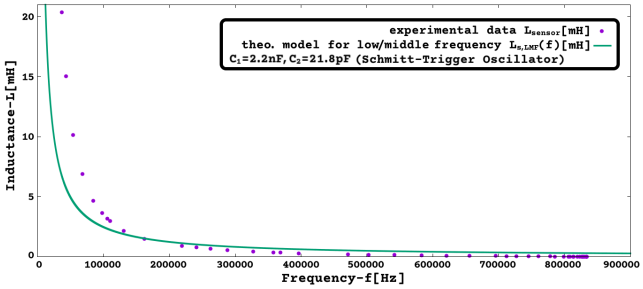

Figure 28: $L_{s,LMF}(f)$ [mH], frequency in [0Hz, 900kHz] (Sch-trig. osc., Multi-Sensor Int. with inductive sensor, LMF approx. function).

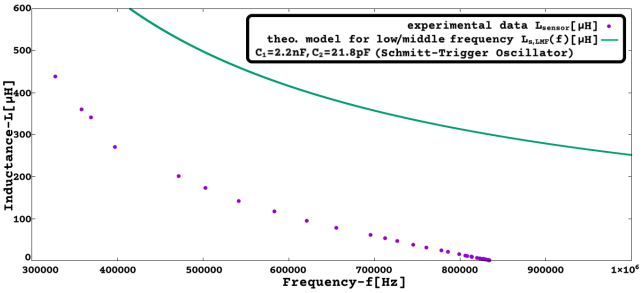

Figure 29: $L_{s,LMF}(f)$ [μH], frequency in [300kHz, 1MHz] (Sch-trig. osc., Multi-Sensor Int. with inductive sensor, LMF approx. function).

significantly displaced above the experimental data for low and middle values of frequency, but for high frequency the plot of $abs(L_{s,HF}(f))$ is much closer to the experimental data and correctly predicts that a value of $L_s = 0$ will result on an oscillation frequency somewhat above 800kHz but lower than 900kHz.

The Fig.28 and Fig.29, shows experimental data for Multiple-Sensor Interface with various inductance values connected as the sensor, and the plot of $L_{s,LMF}(f)$ using (31) with the mentioned values of C_1, C_2, R_2, R_1, H. Observing Fig.28 and Fig.29 is noticeable that $L_{s,LMF}(f)$ follows the experimental data on low and middle frequency (however with some displacement), but for high frequency $L_{s,LMF}(f)$ has a large displacement to the experimental data and fails to predict the frequency at L_s=0.

A way for obtaining a theoretical function (by previously mentioned approximations/simplifications) valid for all values of frequency, that captures the behavior of the Multiple-Sensor Interface with an inductive sensor, is to combine both the expressions $abs(L_{s,HF}(f))$ and $L_{s,LMF}(f)$ into a single function. That function can be obtained for example by multiplying $abs(L_{s,HF}(f))$ with a moderating function that silences it on low and middle frequency and by multiplying $L_{s,LMF}(f)$ with a moderating function that silences it on high frequency, then sum these 2 parts to obtain $L_s(f)$.

A set of 2 good moderating functions, considering the used values of C_1, C_2, R_2, R_1, H, would be for example:
$m_{HF,ef}(f) = (((-1+(e^{(f/100000)-5}))/(1+(e^{(f/100000)-5})))+1)/2$
$m_{LMF,ef}(f) = (((-1+(e^{(-f/100000)+5}))/(1+(e^{(-f/100000)+5})))+1)/2$

These moderating functions are good because:
$m_{HF,ef}(f)$+$m_{LMF,ef}(f)\approx 1$, $\forall f$, and also:
$m_{HF,ef}(f=0)\approx 0$; $m_{HF,ef}(f=900\text{kHz})\approx 1$;
$m_{HF,ef}(f=+\infty)=1$; $m_{LMF,ef}(f=+\infty)=0$;
$m_{LMF,ef}(f=0)\approx 1$; $m_{LMF,ef}(f=900\text{kHz})\approx 0$;
$m_{LMF,ef}(f=500\text{kHz})\approx m_{HF,ef}(f=500\text{kHz})\approx 0.5$.

However the moderating functions $m_{HF,ef}(f)$, $m_{LMF,ef}(f)$ are exponential functions that are undesirably complex and heavy to evaluate; so here is suggested another set of 2 moderating functions that are simpler and faster to evaluate, although the property $m_{HF}(f)$+$m_{LMF}(f)\approx 1$ will only be true on a small frequency range and that will cause some distortion (undesirable change) on the theoretical model. Since the theoretical model is not accurate because of the approximations that were used for obtaining a solution to the initial value problem (that had 3 unknowns k_1, k_2, k_3, but was solved as if had a single unknown), and also knowing that $abs(L_{s,HF}(f))$ is always above the experimental data and that $L_{s,LMF}(f)$ is above the experimental data on a portion of the plot (on this situation for f>250kHz), then can be selected moderating functions that have a 'distortion' that actually approximates(lowers the value of) $abs(L_{s,HF}(f))$ and $L_{s,LMF}(f)$ to the experimental data.

A set of 2 moderating functions that are more simple and fast/easy to evaluate, but 'distort' (lower) the value of $L_s(f)$:

$$m_{HF,f3}(f) = (a_{HF}\cdot f^3)/(1+a_{HF}\cdot f^3) \tag{32}$$

$$m_{LMF,f3}(f) = 1/(1+a_{LMF}\cdot f^3) \tag{33}$$

Also let's have in consideration a frequency value f_0 defined as $abs(L_{s,HF}(f=f_0))$=0 (the frequency where the plot of $abs(L_{s,HF}(f))$ reaches the horizontal axis of $L_s = 0$).

Then, f_0=$(R_1+R_2)/((C_1+C_2)HR_1R_2)$.

So by first determining the frequency f_0 for some selected values of the parameters C_1, C_2, R_2, R_1, H, then is possible to create/define $L_{s,LMF,HF}(f)$ as a 'theoretical' function (by the previously mentioned approximations/simplifications) through $m_{HF,f3}(f)$, $m_{LMF,f3}(f)$, to be valid for all values of frequency:

$$L_{s,LMF,HF}(f) = (L_{s,LMF}(f))\cdot(m_{LMF,f3}(f)) + abs(L_{s,HF}(f))\cdot(m_{HF,f3}(f)) \tag{34}$$

The calculation of a_{HF} and a_{LMF} to create some moderating functions $m_{HF,f3}(f)$, $m_{LMF,f3}(f)$ may be done for example by defining target values of $m_{HF,f3}(f$=$2\cdot f_0/3)$,

$m_{LMF,f3}(f{=}f_0)$, by this method is obtained:

$$a_{HF} = \frac{27(C_1+C_2)^3 H^3 {R_1}^3 {R_2}^3 m_{HF}(f{=}2f_0/3)}{8(R_1+R_2)^3(1-m_{HF}(f{=}2f_0/3))} \quad (35)$$

$$a_{LMF} = \frac{(C_1+C_2)^3 H^3 {R_1}^3 {R_2}^3 (1-m_{LMF}(f{=}f_0))}{(R_1+R_2)^3 m_{LMF}(f{=}f_0)} \quad (36)$$

So the constant a_{HF} may be selected/adjusted so that $m_{HF,f3}(f{=}2{\cdot}f_0/3){=}0.5$, this is the same as to say that a_{HF} will be selected/adjusted so that when frequency is at 2/3 of f_0 then $abs(L_{s,HF})\cdot(m_{HF,f3})$ will be 50% of $abs(L_{s,HF})$.

So the constant a_{LMF} may be selected/adjusted so that $m_{LMF,f3}(f{=}f_0){=}0.01$, this is the same as to say that a_{LMF} will be selected/adjusted so that when frequency is at f_0 then $(L_{s,LMF})\cdot(m_{LMF,f3})$ will be 1% of $(L_{s,LMF})$.

So for this case ($R_1{=}2M\Omega$, $R_2{=}500\Omega$, $C_1{=}2.2$nF, $C_2{=}21.78$pF, $H{=}1.01496$), with $m_{HF,f3}(f{=}2{\cdot}f_0/3){=}0.5$, $m_{LMF,f3}(f{=}f_0){=}0.01$, was selected/adjusted the values: $a_{HF} = 4.834{\cdot}10^{-18}\ s^3$, $a_{LMF} = 1.418{\cdot}10^{-16}\ s^3$ (Fig. 30).

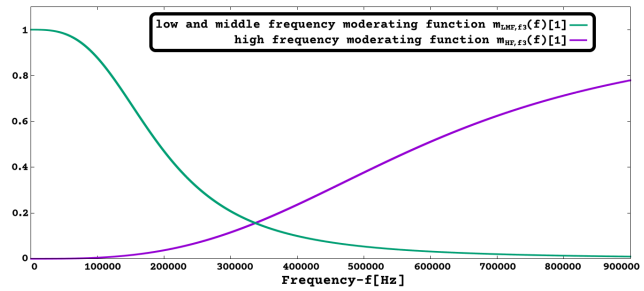

Figure 30: $m_{LMF,f3}(f)$ and $m_{HF,f3}(f)$ [1], frequency in [0Hz, 900kHz].

The Fig. 31 and Fig. 32, shows experimental data for Multiple-Sensor Interface with various inductance values connected as the sensor, and the plot of $L_{s,LMF,HF}(f)$ using (34) with $C_1{=}2.2$nF, $C_2{=}21.78$pF, $R_2{=}500\Omega$, $R_1{=}2M\Omega$, $H{=}1.01496$, $a_{HF} = 4.834{\cdot}10^{-18}\ s^3$, $a_{LMF} = 1.418{\cdot}10^{-16}\ s^3$.

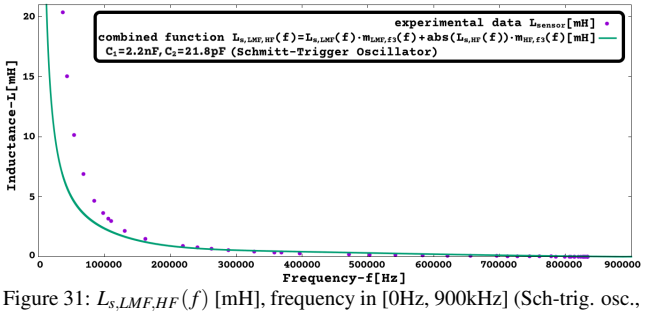

Figure 31: $L_{s,LMF,HF}(f)$ [mH], frequency in [0Hz, 900kHz] (Sch-trig. osc., Multi-Sensor Int. with inductive sensor, LMF and HF combined approx. function, with $C_1{=}2.2$nF, $C_2{=}21.78$pF).

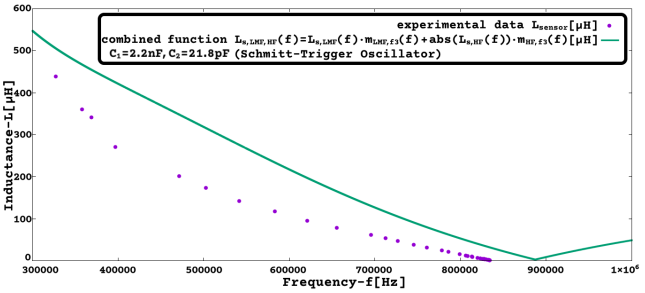

Figure 32: $L_{s,LMF,HF}(f)$ [μH], frequency in [300kHz, 1MHz] (Sch-trig. osc., Multi-Sensor Int. with inductive sensor, LMF and HF combined approx. function, with $C_1{=}2.2$nF, $C_2{=}21.78$pF).

4 Discussion

The experimental data obtained when testing the Multiple-Sensor Interface is in overall close to the values calculated using the formulas obtained from the circuit analysis, as it is visible on the various figures that show the plots of the experimental data along with graphs done using the mentioned formulas. In some graphs, there was a deviance or offset between the theoretical and experimental quantitative values, however the observable deviations are not reason for concern as they never affected the similitude between theoretical and experimental graphs (with exception of Fig.9 and Fig.10 that as explained, when using that specific configuration the device no longer behaves as Pierce oscillator, but instead as a Schmitt Trigger oscillator, as it was shown on later subsections). The information that is made available on the article, besides explaining how the device works, may also be useful for a user of the device/technology for determining if a specific sensor of his interest is compatible/usable when connected to the Multiple-Sensor device, namely by observing on the graphs (or tables), for what range of values (min. and max.) of the sensor electrical quantity (R_s or C_s or L_s) it is verified that a change on the quantity the sensor is measuring will produce/cause also a significant or measurable change of the signal frequency on the output of the oscillator used for sensor interfacing.

4.1 Future Work

Further work related to the sensor interface circuit may be developing a better understanding/prediction of why/when the Multiple-Sensor Interface with inductive sensor changes from working as Pierce oscillator to Schmitt-trigger oscillator depending on the values of C_1 and C_2 capacitors (whose values can be adjusted by jumpers JP.A and JP.B).

Other future work, outside the scope of this article, could be characterizing, testing, and comparing this sensor interface circuit for specific sensor types and/or applications, thus allowing a performance comparison with other technologies on specific use cases.

4.2 Better accuracy on a commercial scenario

A more commercial usage of Multiple-Sensor Interface possibly with better accuracy by using pre-calibrated sensors PCBs, may be:

1- Production of small single sensor PCBs that include: one sensing element (Ex: RTD, LDR, proximity inductive sensor, capacitive humidity sensor, etc ...), the oscillator circuit, and a voltage stabilizer (Ex: Zener diode). The voltage stabilizer is required to obtain a stable/fixed V_{DDS} on the sensor PCB independent of the power supply, that is already set when the producer/seller does the sensor calibration. Also the sensor PCBs should have values of C_1 and C_2 selected/tuned for best measurement range or best accuracy/precision (and so jumpers JPA/JPB not required, or may be soldered/fixed), having as output the oscillator square wave signal.

2- Obtaining a calibration table for the single sensor PCB (pairing output oscillator frequency with measurements by reference calibration instruments), on an appropriate calibration environment done/performed by the producer/seller.

3- Distribution/sale of the sensor PCBs with their own calibration table included. Could be: a calibration table printed

on paper (for example: to be typed by hand on the software/application of the device, or automatically by OCR or QR-code), or as digital file that can be downloaded from the distributor/seller by using a serial number associated with the single sensor PCB.

4- An end user would connect a single sensor PCB to the Multiple-Sensor Interface device (that contains the microcontroller, EEPROM, and USB, RS-485, GPIO interfaces) on one of the frequency measurement channels (and also connect the GND), preferably using the same power supply for both the sensor PCBs and the Multiple-Sensor device. The end-user would import the provided calibration table into the Multiple-Sensor device, using the provided software/application.

Also note that with an external single sensor PCB any oscillator circuit/design may be used as long its output is a square wave signal (that doesn't exceeds the power supply voltage); and also that a much longer distance/cable can be used between the sensor location and the Multiple-Sensor Interface device, since that any parasitic resistance/capacitance/inductance of the cable won't affect the oscillator frequency that will be measured by the device.

The production/sale and usage scenario here described is the author perspective of a modest compromise that could be made on the hardware configurability/versatility (of the single sensor PCB with square wave signal output), that allows a producer/seller to supply ready to use sensors without any changes on the proposed hardware design of the Multiple-Sensor Interface (since it already includes 4 channels dedicated to measuring frequency of an external signal) and so without restricting the end-user ability to use any sensors it wishes or even a custom made sensor for a very specific use/application.

4.3 About $C_s(f)<0$ on Multi-Sensor with capacitive sensor

About $C_s(f)<0$ have in mind the Multiple-Sensor with capacitive sensor is studied on transient behavior (relaxation oscillator), where 'frequency' is a measure of the speed of charge and discharge on C_1; and also of how fast the transient circuit analysis alternates between v_o=V_{DDS} and v_o=0.

To understand why a normal capacitor may behave as a negative capacitance when connected as the sensor of the Multiple-Sensor Interface (this is, a way to check that $C_s(f)<0$ is possible/expected), is important to highlight some things already explored on the previous sections:

1) C_1=C_2, $R_1 \gg R_2$.

2) The primary path (always available) to charge C_1 is through R_1, the primary path (always available) to charge C_2 is through R_2, since $R_1 \gg R_2$ and C_1=C_2 this implies that capacitor C_2 will charge/discharge much faster(takes less time) than capacitor C_1.

3) The purpose of sensor C_s on this circuit is to act as a variable impedance that can establish an alternative path on the circuit ($V_o \rightarrow R_2 \rightarrow C_s \rightarrow C_1$) to charge/discharge capacitor C_1; so $C_s \nearrow \Rightarrow |Z_s| \searrow \Rightarrow R_{approx} \searrow \Rightarrow \tau_2 \searrow \Rightarrow$ C_1charges faster.

4) No matter how small $|Z_s|$ may be the capacitor C_2 will always charge/discharge faster than capacitor C_1, and on the limit where $|Z_s|$=0 the capacitors C_1 and C_2 will be charged/discharged simultaneously.

5) The capacitors C_1, C_2, C_s have same working principles, but consequence of their position within the circuit they serve different functions; so C_1 and C_2 are working as storage of electrical charge (Ex: they start discharged and end charged), while C_s is working as a connection with 'impedance' against charge flow (Ex: starts discharged and will end discharged, that is: $v_s(t=0)=0$ and $v_s(t=+\infty)=0$).

For the following discussion was used as definition of capacitance the formula $C_s = i_s/(dv_s/dt)$, where the $|C_s| = |Q_s|/|v_s|$ (C_s: [F] farad; Q_s: [C] coulomb; v_s: [V] volt), and since the only purpose is to show how C_s can be a negative number it was used the approximate expression $C_s \approx \overline{i_s}/(\Delta v_s/\Delta t)$ that provides exactly the same sign as the exact formula; the $\overline{i_s}$ is the average(mean) value of i_s between t=t_1 and t=t_2 . To show is possible $C_s<0$ were considered qualitative relations of the circuit electrical parameters on the RC network of the oscillator, the relevant electrical parameters and their variation between t=t_1 and t=t_2 is represented in Fig.33.

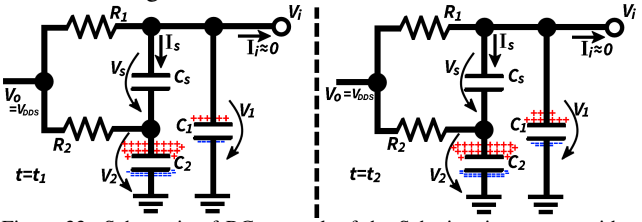

Figure 33: Schematic of RC network of the Schmitt-trigger osc. with a representation of electrical charge on C_1, C_2 on t=t_1 and t=t_2.

It were assumed symbolic values for the voltages on the circuit, used as specimen values to determine how fast a voltage is changing between t_1 and t_2 time moments. So for representing a small amount of electrical charge are used the symbols: [+] for positive charge and [-] for negative charge, since already stated $C_1 = C_2$ for each additional amount of [+] and [-] charge stored on each plate (of C_1 or C_2) will cause an increase of capacitor voltage that will be represented as $[+\underline{v}]$, where $C_1 = C_2 = [+]/[+\underline{v}]$.

As visible in Fig.33, V_o=V_{DDS}≈+4.18V, and so V_{DDS} will eventually be the voltage on C_1 and C_2 when t→∞. For making visual on the schematic the charging process, the charge accumulated in C_1, C_2 was divided in 20 sets, each represented by [+], [-]; and for each set of accumulated charge is associated a corresponding increase in voltage of $[+\underline{v}]$, and so $[+\underline{v}] = V_{DDS}/20$.

Accordingly in Fig.33 is represented that C_2 is charged to near the final value (V_{DDS}) during the interval $[0;t_1]$ while C_1 charges much slower. During interval $[t_1;t_2]$ is visible that C_2 increased its charge only by 1[+] becoming charged to approximately(or practically) its final value($v_2 \approx V_{DDS}$), whether C_1 is still charging and v_1 is far from its final value(V_{DDS}), but interestingly v_1 is now increasing faster than v_2, because v_2 already reached its final value, this is $dv_1/dt > dv_2/dt, \forall t \in [t_1;t_2]$. The specimen values here mentioned are in line with the exponential function typical of capacitors charging through a resistor, where lets say a capacitor initially charges very fast, when has some charge stored it charges more slowly, and when close to being full it charges very slowly (where full means the capacitor voltage is close to power supply voltage).

4.3.1 Voltage and current specimens for t=t_1

So looking at the schematic on left side of Fig.33 is visible C_1 and C_2 are charging and for t=t_1 the charge on C_1 is 5[+] and on C_2 is 19[+], so capacitor C_2 is almost charged while C_1 is still charging. Capacitor C_1 is charging through the path $V_o \rightarrow R_1 \rightarrow C_1$ but mainly is charging through path $V_o \rightarrow R_2 \rightarrow C_s \rightarrow C_1$, since $v_2 > v_1$ then $i_s(t{=}t_1) < 0$.
For t=t_1, Q_1=5[+], Q_2=19[+], then v_1=5[+$\underline{v}$], v_2=19[+$\underline{v}$], since v_s=$v_1 - v_2$ then $v_s(t{=}t_1)$=5[+$\underline{v}$]−19[+$\underline{v}$]=−14[+$\underline{v}$].

4.3.2 Voltage and current specimens for t=t_2

So looking at the schematic on right side of Fig.33 is visible C_1 and C_2 are charging and for t=t_2 the charge on C_1 is 9[+] and on C_2 is 20[+], so capacitor C_2 is fully charged while C_1 is still charging. Capacitor C_1 is charging through the path $V_o \rightarrow R_1 \rightarrow C_1$ but mainly is charging through path $V_o \rightarrow R_2 \rightarrow C_s \rightarrow C_1$, since $v_2 > v_1$ then $i_s(t{=}t_2) < 0$.

For t=t_2, Q_1=9[+], Q_2=20[+], then v_1=9[+$\underline{v}$], v_2=20[+$\underline{v}$], since v_s=$v_1 - v_2$ then $v_s(t{=}t_2)$=9[+$\underline{v}$]−20[+$\underline{v}$]=−11[+$\underline{v}$].

4.3.3 Sign of C_s as calculated from v_s and i_s during $[t_1;t_2]$

The schematics in Fig.33 refer to a charging cycle of the Schmitt Trigger Oscillator. Also $t_2 > t_1 \rightarrow \Delta t > 0$.

For $t \in [t_1;t_2]$ the capacitor C_1 is being charged through the path $V_o \rightarrow R_2 \rightarrow C_s \rightarrow C_1$ and so $i_s(t) < 0, \forall t \in [t_1;t_2] \Rightarrow \overline{i_s} < 0$. Also Δv_s between t_1 and t_2 is Δv_s=$v_s(t{=}t_2) - v_s(t{=}t_1)$ = −11[+$\underline{v}$]−(−14[+$\underline{v}$])=3[+$\underline{v}$], so $\Delta v_s > 0$ between t_1 and t_2.

So concluding between t_1 and t_2, $\Delta t > 0$, $\Delta v_s > 0$, $\overline{i_s} < 0$ $\Rightarrow C_s < 0$ accordingly with $C_s \approx \overline{i_s}/(\Delta v_s/\Delta t)$.

4.4 Comparison to known cases of negative capacitance

Aspects of Multiple Sensor Interface circuit possibly related to negative capacitance phenomenon:
1- Use of Schmitt-trigger 'NOT' gate which exhibits hysteresis on its $v_o(v_i)$ graph.
2- Multiple Sensor Interface with a capacitive sensor operates under transient(time domain), step change of voltage caused by its 'NOT' gate(Schmitt-trigger) alternating between 0V and $+V_{DDS}$ (relaxation oscillator).

Negative capacitance phenomenon is reported in some scientific articles/texts, and interestingly with some coincidence to the 2 aspects mentioned above. Quotes:
1- "Effective negative capacitance has been postulated in ferroelectrics because there is hysteresis in plots of polarization-electric field.", article "Towards steep slope MOSFETs using ferroelectric negative capacitance", by A. O'Neill, year 2014 [5].
2- "The phenomenon of negative capacitance, which has been reported in a variety of situations involving electrolytic as well as electronic systems, ... It is suggested that the physically correct approach lies in the analysis of the corresponding time-domain behavior under step function bias, which involves a current initially falling and then rising gradually over a period of time before finally decaying to zero.", article "The physical origin of negative capacitance", by A. K. Jonscher, year 1986 [6].

5 Conclusions

The author theoretically demonstrated a more versatile design for use with sensor applications, also was provided experimental data that corroborates the presented theory. The motivation of the author was to make available an electronics design that could be more sustainable in terms of life-cycle duration, by making a design more customizable by the user and also not closed/locked to a specific application/purpose. No warranty is given that the design can provide accuracy or convenience to a specific application/use; as the article is focused on showing how a versatile design can be achieved.

Conflicts of interest

The author declares no conflict of interest.

Acknowledgments

I thank in general, to the Open-Source community for making available technology that everyone can use and build-on freely, thus inspiring me to also release this project as Open-Source. Also thanks to GNUplot software, that was used for drawing the plots in this article [15] .

Also thanks to Wolfram Research Inc. for providing Wolfram Mathematica® for Raspberry Pi with RaspberryPi-OS and so making their software easily available to use by everyone, it was used version 12 for obtaining/solving inverse function and algebraic manipulation of long equations [16] .

Appendix A. Experimental Datasets

Experimental data obtained (Fig.5) by using fixed value components connected as the sensor on the device. Were used arrays(PCBs) with inductors, resistors, capacitors that allow to obtain various different values just by changing a jumper/switch, and also single components (including in series or parallel association). The tolerance of the PCB components is: ±5% for R1, R2, and ±10% for C1, C2.

A.1 Frequency measurement by Multi-Sensor

The Multiple-Sensor device measures frequency using a counter inside the microcontroller and has some accuracy and range limitations, it can measure up to 3MHz (higher frequency causes counter overflow). The Multiple-Sensor device was tested with a square wave signal from the signal generator JDS6600 (by Joy-IT, frequency accuracy: ±20ppm).

The Multiple-Sensor device measurement accuracy (percentage error) of frequency, is worst at low frequencies with 9% error at 100Hz and 0.7% error at 1kHz, above 5kHz the error was always smaller than 0.2% (ignoring any accuracy error by JDS6600 used as reference). The Multiple-Sensor device measurement precision (variation) for frequency was worst at low frequencies with 5% variation at 300Hz, above 1500Hz was always smaller than 1%, and above 15kHz was always smaller than 0.1%.

A.2 Experimental data on Multi-Sensor Int

- Reference instruments:

The measurements of inductance(L_s) and capacitance(C_s) were obtained using the LCR meter TH2821A (by Tonghui, basic accuracy 0.3%), configured to 10kHz test signal (for L_s>202mH was used 1kHz test signal).

The measurements of resistance(R_s) were obtained using the meter UT603 (by UNI-T, accuracy: 0.8% for R⩽2MΩ; 2% for R>2MΩ).

- Units: Hz=hertz, H=henry, Ω=ohm, F=farad.

- Jumper Configurations:

[a](JPA on, JPB off): C_1=2.2nF; C_2=21.8pF.

[b](JPA off, JPB on): C_1=21.8pF; C_2=2.2nF.

[c](JPA on, JPB on): C_1=2.2nF; C_2=2.2nF .

Here is made available, the sets of experimental data that were used for drawing the plots of $L_s(f)$, $R_s(f)$, $C_s(f)$, these are the measured values of inductance, resistance, capacitance paired with measured frequency on the Multiple Sensor Interface device.

On Appendixes A and B the symbols R_s, C_s, L_s usually are/mean the same as R_{sensor}, C_{sensor}, L_{sensor} and refer to measured values by the reference instruments. So on Ap. A and Ap. B, unless an explicit reference to a theoretical function is made, then R_s=R_{sensor}, C_s=C_{sensor}, L_s=L_{sensor}.

Table 1: Set of experimental data for C_s vs. frequency

C_s[nF] Capacitance	f[Hz][c] JPA on, JPB on	C_s[nF] Capacitance	f[Hz][c] JPA on, JPB on
0	229	4.97	373045
0.152	321	5.97	385032
0.310	458	6.95	394283
0.568	2614	7.94	400750
0.615	54570	8.98	405766
0.689	110286	10.07	411246
0.776	140178	12.04	418028
1.015	186522	15.02	426040
1.34	231460	20.02	433089
1.58	255526	24.97	437446
1.79	271015	29.68	440382
2.00	285020	34.62	442584
2.56	314530	39.43	444235
2.99	329820	44.38	445688
3.98	356012	49.38	446712

Precision error(maximum frequency variation):
±3kHz (600pF⩽C_s<1.6nF); ±1kHz (C_s⩾21nF);
±2kHz (1.6nF⩽C_s<21nF); ±50Hz (C_s<600pF).

Table 2: Set of experimental data for L_s vs. frequency

$L_s[\mu H]$ Inductance	f[Hz][a] JPA on, JPB off	f[Hz][b] JPA off, JPB on	f[Hz][c] JPA on, JPB on
1.21	834161	879205	446590
1.40	833855	885138	476589
1.65	833350	888501	473393
1.85	833014	887049	458577
2.51	831302	881055	494096
3.09	829880	892844	474739
3.80	828045	898700	467354
4.10	827433	891116	466711
4.70	826011	881239	496405
5.87	823121	873380	519263
7.32	819681	915412	577595
8.76	813947	864236	591646
9.70	813397	858548	615743
11.77	808321	936894	1432920
12.84	805905	934723	1357220
15.76	799009	895932	1251070
21.39	785691	931940	1090760
24.49	778123	978330	1011830
31.80	760632	1056660	889633
38.61	745112	1193360	809559
46.70	726580	1369450	736014
53.44	712070	2853370	690970
61.30	695603	2662840	639014
78.30	655604	2332760	568099
95.34	620697	2103380	509845
117.60	583023	1899190	464617
142.28	541388	1722220	420062
173.50	502398	1575330	382571
201.50	471222	1464370	354070
271.46	396546	1201810	292482
341.8	368641	1112820	271168
360.6	357938	1085180	261856
438.7	327053	994721	239762
558.1	287880	868105	212362
660.7	262804	794697	194290
777.6	241031	737803	178480
921.2	218738	677591	163587
1491	161768	606844	124338
2171	130897	499264	102978
2976	109912	446452	87856
3170	105439	406011	84614
3640	97779	383305	79110
4646	84110	319423	69783
6880	68162	282360	57750
10140	54034	224090	47230
15040	43377	192088	38790
20375	36588	171981	33683

Precision error(maximum frequency variation):
±2kHz (at high 'f[Hz]'); ±300Hz (at low 'f[Hz]');
±5kHz (2.85MHz↔1.36MHz; at [b] JPA off, JPB on).

Table 3: Set of experimental data for R_s vs. frequency

$R_s[\Omega]$ Resistance	f[Hz]^c JPA on, JPB on	$R_s[\Omega]$ Resistance	f[Hz]^c JPA on, JPB on	$R_s[\Omega]$ Resistance	f[Hz]^c JPA on, JPB on	$R_s[\Omega]$ Resistance	f[Hz]^c JPA on, JPB on
0	456284	577	231735	4180	79553	28900	16666
1.2	454678	597	228447	4380	77107	29900	16176
2.2	453975	617	225252	4580	74783	31900	15244
3.2	453149	637	222178	4780	72612	33900	14418
4.2	452400	657	219228	4980	70593	35900	13669
5.2	451605	677	216353	5180	68682	37800	13027
6.2	450718	697	213647	5380	66863	39800	12430
7.2	449923	717	210971	5580	65135	41800	11880
8.2	449067	736	208402	5770	63514	43800	11375
9.2	448272	756	205910	5970	61985	45800	10917
10.2	447385	776	203464	6170	60517	47800	10488
15.2	443226	796	201139	6370	59111	49800	10091
20.1	439144	816	198877	6570	57765	54800	9235
25.1	435183	836	196659	6770	56511	59800	8531
30.1	431269	856	194504	6970	55288	64800	7904
35.1	427447	876	192409	7170	54126	69700	7385
40.0	423655	896	190406	7370	53010	74700	6926
45.0	420016	916	188418	7570	51940	79700	6513
50.0	416407	936	186476	7760	50915	84600	6146
55.0	412845	955	184611	7960	49952	89600	5825
60.0	409359	975	182776	8460	47643	94600	5550
65.0	406010	996	180865	8960	45548	99400	5320
69.9	402601	1096	172578	9460	43622	109400	4862
74.9	399328	1195	165208	9960	41879	119300	4479
79.9	396209	1295	158603	10460	40243	129300	4158
84.9	393060	1394	152594	10960	38760	139300	3883
89.9	390017	1494	147150	11460	37353	149300	3623
94.8	387005	1593	142135	11960	36053	159200	3440
99.9	383396	1693	137548	12450	34861	169200	3256
119.7	372387	1792	133298	12960	33714	179100	3073
139.7	361700	1892	129353	13450	32659	189100	2935
159.6	351608	1992	125699	13950	31680	199100	2798
179.5	342205	2090	122258	14450	30732	299000	1972
199.5	333306	2190	119017	14950	29861	398000	1544
219	325050	2290	115974	15440	29035	498000	1284
239	317236	2390	113115	15940	28255	597000	1100
259	309836	2490	110409	16440	27522	697000	978
279	302879	2590	107855	16940	26818	796000	886
299	296289	2690	105424	17430	26145	896000	825
319	290112	2790	103115	17930	25503	995000	779
339	284225	2890	100914	18430	24907	1495000	596
359	278614	2990	98819	18930	24326	1993000	504
378	273308	3090	96831	19420	23775	2490000	458
398	268278	3190	94905	19940	23271	3090000	412
418	263462	3290	93070	20900	22292	4080000	366
438	258829	3390	91327	21900	21375	5080000	351
458	254471	3490	89645	22900	20549	6070000	336
478	250251	3580	88024	23900	19769	7070000	321
498	246214	3680	86464	24900	19066	8050000	321
518	242361	3780	84966	25900	18393	9040000	305
538	238646	3880	83529	26900	17782		
557	235144	3980	82153	27900	17201		

Precision error(maximum frequency variation):
$\pm$1kHz(at low R_s); $\pm$300Hz(at 30kΩ); $\pm$100Hz(at high R_s).

Appendix B. Additional Experimental Datasets

Here are additional experimental datasets, these are measured values of inductance, resistance, capacitance paired with measured frequency by the Multi-Sensor device. These additional experimental datasets were not used on any previous plot/graph displayed along the article, and are here made available to give additional evidence, also with graphs comparing them against the respective theoretical results. The symbols R_s, C_s, L_s are/mean the same as on Appendix A.

- Reference instruments: Same as on Appendix A.

- Jumper Configurations/Capacitor Values:

[d](JPA on, JPB off): C_1=93nF (≈91nF+2.2nF); C_2=21.8pF.
[e](JPA off, JPB on): C_1=21.8pF; C_2=93nF (≈91nF+2.2nF).
[f](JPA on, JPB on): C_1=93nF; C_2=93nF (≈91nF+2.2nF).

- Note: The configurations/designs where the references C_1 and/or C_2 are 93nF(≈91nF//2.2nF=91nF+2.2nF), were obtained by connecting a 91nF capacitor in parallel with the 2.2nF capacitor already on the Multi-Sensor PCB.

The Fig.34 shows experimental data for Multi-Sensor device with various resistance values connected as the sensor and also $R_s(f)$ using (9) with C_1=C_2=93nF, R_1=2$M\Omega$, R_2=500Ω, V_T^-=1.2V, V_T^+=2.2V, V_{DDS}=4.18V, H=1.01496.

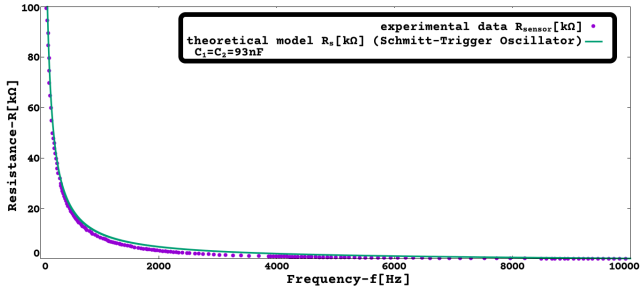

Figure 34: $R_s(f)$ [kΩ], with C_1=C_2=93nF, frequency in [0Hz, 10kHz] (Schmitt-trigger osc., Multiple-Sensor Int. with resistive sensor).

The Fig.35 and Fig.36 shows experimental data for Multi-Sensor device with various capacitance values connected as sensor and $|C_s(f)|$ using (17) with C_1=C_2=93nF, V_T^-=1.2V, V_T^+=2.2V, V_{DDS}=4.18V, R_1=2$M\Omega$, R_2=500Ω, H=1.01496.

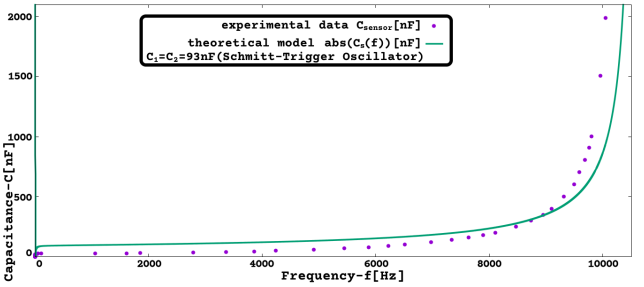

Figure 35: $|C_s(f)|$ [nF], with C_1=C_2=93nF, frequency in [0Hz, 10500Hz] (Schmitt-trigger osc., Multi-Sensor with capacitive sensor)

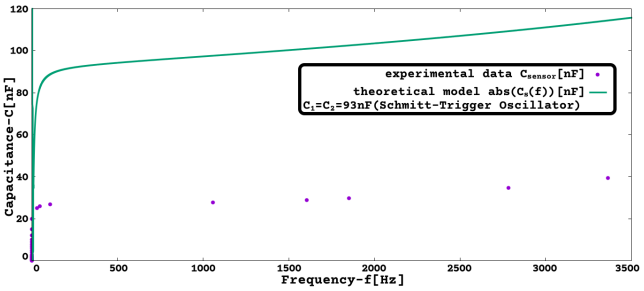

Figure 36: $|C_s(f)|$ [nF], with C_1=C_2=93nF, frequency in [0Hz, 3500Hz] (Schmitt-trigger osc., Multi-Sensor with capacitive sensor)

The Fig.37 and Fig.38 shows experimental data for Multiple-Sensor device with various inductance values connected as the sensor, and also $L_{s,LMF,HF}(f)$ using (34) with C_1=93nF, C_2=21.78pF, R_1=2$M\Omega$, R_2=500Ω, H=1.01496, $m_{HF,f3}(f$=2·$f_0/3)$=0.5, $m_{LMF,f3}(f$=$f_0)$=0.01, a_{HF} = 3.548·10^{-13} s^3, a_{LMF} = 1.041·10^{-11} s^3.

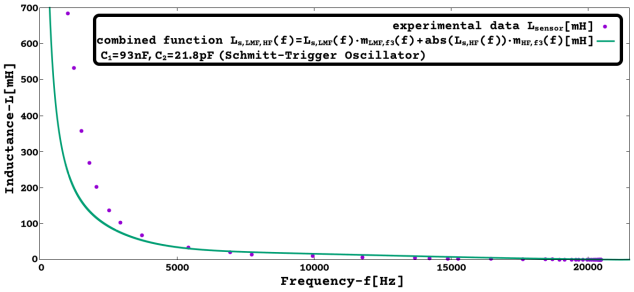

Figure 37: $L_{s,LMF,HF}(f)$ [mH], with C_1=93nF, C_2=21.78pF, frequency in [0Hz, 21500Hz] (Sch-trig. osc., Multi-Sensor w. inductive sensor)

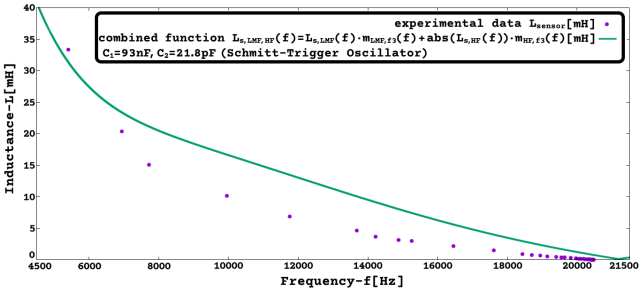

Figure 38: $L_{s,LMF,HF}(f)$ [mH], with C_1=93nF, C_2=21.78pF, frequency in [4500Hz, 21500Hz] (Sch-trig. osc., Multi-Sensor w. inductive sensor)

Table 4: Additional set of experimental data for C_s vs. frequency

C_s[nF] Capacitance	f[Hz][f] JPA on, JPB on C_1=C_2=93nF	C_s[nF] Capacitance	f[Hz][f] JPA on, JPB on C_1=C_2=93nF
0.152	0	49.38	4235
0.568	0	59.39	4908
1.015	0	69.62	5443
1.58	0	79.96	5871
2.00	0	90.38	6223
2.99	0	100.38	6513
3.98	0	120.27	6972
4.97	0	139.62	7339
5.97	0	159.66	7629
7.94	0	180.22	7889
10.07	0	201.13	8103
12.04	0	250.42	8470
15.02	0	300.0	8730
20.02	0	349.3	8944
24.97	30	400.2	9097
25.89	45	502.9	9311
26.87	107	603.7	9495
27.86	1055	706.7	9586
28.87	1605	806.5	9678
29.68	1850	909.1	9755
34.62	2782	1003.5	9800
39.43	3363	1507.3	9953
44.38	3853	1991.7	10045

Precision error(maximum frequency variation):
±15Hz (C_s⩽34.62nF); ±50Hz (100.38nF<C_s⩽180.22nF);
±30Hz (34.62nF<C_s⩽100.38nF); ±100Hz (C_s>180.22nF).

Table 5: Additional set of experimental data for R_s vs. frequency

$R_s[\Omega]$ Resistance	f[Hz]^f JPA on, JPB on C_1=C_2=93nF	$R_s[\Omega]$ Resistance	f[Hz]^f JPA on, JPB on C_1=C_2=93nF	$R_s[\Omega]$ Resistance	f[Hz]^f JPA on, JPB on C_1=C_2=93nF	$R_s[\Omega]$ Resistance	f[Hz]^f JPA on, JPB on C_1=C_2=93nF
0.1	10198	577	4999	4180	1697	28900	336
1.2	10183	597	4923	4380	1651	29900	336
2.2	10167	617	4862	4580	1590	31900	321
3.2	10152	637	4785	4780	1544	33900	290
4.2	10137	657	4724	4980	1513	35900	275
5.2	10106	677	4663	5180	1467	37800	275
6.2	10091	697	4587	5380	1421	39800	259
7.2	10076	717	4541	5580	1376	41800	244
8.2	10045	736	4479	5770	1345	43800	229
9.2	10030	756	4418	5970	1330	45800	229
10.2	10014	776	4357	6170	1284	47800	214
15.2	9923	796	4311	6370	1253	49800	198
20.1	9816	816	4265	6570	1223	54800	183
25.1	9724	836	4220	6770	1192	59800	168
30.1	9632	856	4174	6970	1162	64800	152
35.1	9540	876	4128	7170	1146	69700	137
40.0	9449	896	4082	7370	1131	74700	137
45.0	9357	916	4036	7570	1100	79700	137
50.0	9281	936	3990	7760	1085	84600	122
55.0	9204	955	3944	7960	1055	89600	122
60.0	9128	975	3898	8460	1009	94600	107
65.0	9036	996	3868	8960	963	99400	91
69.9	8944	1096	3700	9460	917	109400	91
74.9	8883	1195	3531	9960	871	119300	91
79.9	8807	1295	3394	10460	856	129300	76
84.9	8715	1394	3256	10960	825	139300	76
89.9	8669	1494	3134	11460	779	149300	61
94.8	8577	1593	3027	11960	764	159200	61
99.9	8485	1693	2935	12450	733	169200	45
119.7	8210	1792	2843	12960	703	179100	45
139.7	7966	1892	2752	13450	688	189100	45
159.6	7736	1992	2675	13950	672	199100	45
179.5	7522	2090	2614	14450	642	299000	30
199.5	7293	2190	2522	14950	626	398000	15
219	7109	2290	2476	15440	611	498000	15
239	6926	2390	2400	15940	596	597000	0
259	6758	2490	2339	16440	581	697000	0
279	6605	2590	2293	16940	565	796000	0
299	6467	2690	2247	17430	550	896000	0
319	6314	2790	2201	17930	535	995000	0
339	6192	2890	2155	18430	519	1495000	0
359	6054	2990	2110	18930	504	1993000	0
378	5932	3090	2064	19420	504	2490000	0
398	5825	3190	2018	19940	489	3090000	0
418	5718	3290	1972	20900	458	4080000	0
438	5611	3390	1941	21900	443	5080000	0
458	5504	3490	1911	22900	428	6070000	0
478	5412	3580	1880	23900	412	7070000	0
498	5320	3680	1834	24900	397	8050000	0
518	5229	3780	1804	25900	382	9040000	0
538	5152	3880	1788	26900	366		
557	5091	3980	1743	27900	351		

Precision error(maximum frequency variation):
$\pm$300Hz(at low R_s); $\pm$50Hz(at 996Ω); $\pm$30Hz(at high R_s).

Table 6: Additional set of experimental data for L_s vs. frequency

$L_s[\mu H]$ Inductance	f[Hz][d] JPA on, JPB off C_1=93nF, C_2=21.8pF	f[Hz][e] JPA off, JPB on C_1=21.8pF, C_2=93nF	f[Hz][f] JPA on, JPB on C_1=93nF, C_2=93nF
1.21	20458	20503	10259
1.85	20412	20519	10259
3.09	20412	20488	10259
4.70	20442	20503	10259
7.32	20458	20503	10259
9.70	20442	20519	10244
15.76	20458	20503	10259
21.39	20472	20503	10244
24.49	20458	20503	10274
38.61	20396	20503	10229
46.70	20366	20503	10274
53.44	20335	20503	10320
61.30	20320	20503	10091
78.30	20274	20503	10473
95.34	20228	20503	9984
117.60	20182	20534	10473
142.28	20106	20503	10488
173.50	20045	20503	9892
201.50	19968	20534	9907
271.46	19815	20427	10917
341.8	19647	20503	10229
360.6	19555	20595	10045
438.7	19403	20565	10657
558.1	19143	20519	10366
660.7	18944	20626	9724
777.6	18699	20503	9128
921.2	18439	20503	8669
1491	17614	20687	18072
2171	16452	20763	14877
2976	15259	20595	12751
3170	14877	20779	12109
3640	14219	20549	11284
4646	13684	20870	9953
6880	11758	20779	8394
10140	9953	20213	6972
15040	7721	20962	5764
20375	6941	20580	4923
33370	5412	20794	3853
68050	3715	23286	2752
102950	2935	63744	2247
136900	2522	62276	1941
202650	2064	43408	1651
269650	1804	37888	1452
358300	1513	21100	1162
532200	1238	21008	1009
684100	1024	20870	825

Precision error(maximum frequency variation):
±300Hz (at high 'f[Hz]'); ±100Hz (at low 'f[Hz]');
±2kHz ([37888Hz;63744Hz]; at [e] JPA off, JPB on).

Appendix C. LDR Sensor Dataset

The A906013 LDR sensor has the following electrical parameters specified by the manufacturer(PerkinElmer/Excelitas) [21]:
R(Illum=10[lx]) is between 27kΩ (min.) and 94kΩ (max.); R(Illum=100[lx]) = 8kΩ (typical value) ; λ_{peak}=600nm (λ_{peak} is the wavelength of light the LDR sensor is most sensitive to); R(Illum=0, after 1s)>0.5MΩ ; R(Illum=0, after 5s)>1.5MΩ; $\gamma_{10/100}$ = 0.8 (typical value).

- Reference instruments:

For obtaining the calibration table of the A906013 LDR sensor on the Multiple-Sensor device it was used as a reference device the Mastech MS6610 luxmeter; the MS6610 luxmeter has the maximum sensitivity at 570nm wavelength, it has an accuracy of $\pm(5\% + 2digits)$, with a resolution (value per digit) of: [0; 1999 [lx]]: 1 [lx]; [2000 [lx]; 19990 [lx]]: 10 [lx]; [20000 [lx]; 50000 [lx]]: 100 [lx].

- Jumper Configurations:

[c](JPA on, JPB on): C_1=2.2nF; C_2=2.2nF .

- Units: Hz=hertz, lx=lux.

Here is made available the calibration of a LDR sensor (Ref: A906013) connected on the Multiple-Sensor Interface.

Table 7: Set of exp. data of LDR sensor for Illuminance[lx] vs. frequency

$Illum$[lx] ref. MS6601	f[Hz][c] (LDR) JPA on, JPB on	$Illum$[lx] ref. MS6601	f[Hz][c] (LDR) JPA on, JPB on
0	244	1485	165972
1	2507	1660	173663
3	6284	1880	189030
10	11788	1985	193433
15	16345	2160	198678
25	23026	2400	205650
30	25320	2930	217530
48	32644	3950	232041
77	44172	5000	244640
100	49768	6000	252651
122	56404	6950	261810
145	63835	8100	267620
173	67346	9650	275877
205	75456	11000	281121
251	81847	12050	286595
300	90180	13350	291702
398	102580	15500	297130
450	107641	17250	300846
512	113375	19000	305205
590	120378	22600	311227
650	124032	25600	315707
715	129124	28600	319469
820	135591	30300	320891
925	141218	33400	325050
1072	147105	37000	328750
1200	155682	39800	333459
1365	162196	48000	340600

Precision error(maximum frequency variation):
±3kHz (1k[lx]$\leqslant Illum <$10k[lx]); ±6kHz ($Illum \geqslant$10k[lx]); ±1kHz (10[lx]$\leqslant Illum <$1k[lx]); ±200Hz ($Illum <$10[lx])

Appendix D. LDR Sensor Model Fitting and Error

Here is shown how the theoretical model of $R_s(f)$, can be combined with a theoretical model of $R_{LDR}(Illum_{LDR})$ of the LDR sensor, to obtain a theoretical function of $Illum_{LDR}(f)$ of the LDR sensor plus the Multiple-Sensor interface, that can be fitted to a small experimental dataset, then obtaining a function that can generate values of $Illum_{LDR}$ versus frequency that are close/similar to the experimental results.

The used model for the LDR sensor is the same type of model mentioned on the datasheet of the LDR sensor (by

PerkinElmer/Excelitas), where the relation between the sensor resistance (R_{LDR}) and the Illuminance (E_{vLDR}) is approximated by a straight line on a logarithmic scale plot (that is, $log(R_{LDR})$ vs $log(E_{v\_LDR})$) is approximately a straight line), the slope of the straight line can be defined by a constant γ where the manufacturer provides an aproximated value of by calculating its value on 2 reference values of Illuminance, typically at 10lx and 100lx.

The equation for the LDR sensor model used here is:

$$R_{LDR}(E_{v\_LDR}) = R_{LDR\_0}\left(\frac{E_{v\_REF}}{E_{v\_LDR}+E_{v\_REF}}\right)^{\gamma} \quad (37)$$

$$\leftrightarrow \quad \gamma = \frac{log(R_{LDR}/R_{LDR\_0})}{log(E_{v\_REF}/(E_{v\_LDR}+E_{v\_REF}))}$$

$$\rightarrow E_{v\_LDR}(R_{LDR}) = E_{v\_REF}\left(\left(\frac{R_{LDR}}{R_{LDR\_0}}\right)^{-1/\gamma} - 1\right).$$

The γ equation becomes equal to what is mentioned in the LDR sensor datasheet if $E_{v\_LDR} \gg E_{v\_REF}$, then:

$$R_{LDR}(E_{v\_LDR}) \approx R_{LDR\_0}\left(\frac{E_{v\_REF}}{E_{v\_LDR}}\right)^{\gamma}$$

$$\leftrightarrow \quad \gamma \approx \frac{log(R_{LDR}/R_{LDR\_0})}{log(E_{v\_REF}/E_{v\_LDR})} \quad .$$

The equation (37) of $E_{v\_LDR}(R_{LDR})$ can be combined with equation (9) of $R_s(f)$ thus obtaining:

$$E_{v\_LDR}(f) \approx E_{v\_REF}\left(\left(\frac{(C_1+C_2)R_2R_1Hf-R_2-R_1}{R_{LDR\_0}(C_2R_2Hf-1)(C_1R_1Hf-1)}\right)^{-1/\gamma} - 1\right) \quad (38)$$

The figures Fig. 39, Fig. 40 are the result of fitting the model function $E_{v\_LDR}(f)$, to the points: (244Hz, 0.01 [lx]), (11788Hz, 10 [lx]), (25320Hz, 30 [lx]), (49768Hz, 100 [lx]), (155682Hz, 1200 [lx]), (232041Hz, 3950 [lx]), (281121Hz, 11000 [lx]), (320891Hz, 30300 [lx]); obtaining the fitted parameter values: γ=0.705486; R_{LDR_0}=559200 [Ω]; E_{v_REF}=0.0362818 [lx]; C_1=4.90986·10^{-9} [F]; C_2=-2.174·10^{-9} [F]; R_1=2.4932·10^6 [Ω]; R_2=636.074 [Ω]; H=1.52273. The point at 244Hz was changed from 0[lx] to 0.01[lx] as it may facilitate/improve the model function fit.

On figure Fig. 41 is shown the relative error in percentage [%] of the fitted model function $E_{v\_LDR}(f)$ when compared with the full experimental dataset of the LDR sensor plus Multiple-Sensor interface; the relative error is calculated by subtracting the value of fitted theoretical function ($E_{v\_LDR}(f)$) from the experimental value of E_{v_LDR}, and then dividing by the experimental value of E_{v_LDR}.

On Fig. 41 is visible that for the point (244Hz, 0.01 [lx]) the relative error is very large (if calculated is about -200%), that occurs because for that point where the Illuminance is 0 [lx] (or 0.01 [lx] as used for the model fitting) the calculation of the relative error on that experimental data point is dividing the absolute error by a number that is very close to zero, thus the relative error will be larger regardless if the absolute error has a reasonable/acceptable value for a function of $E_{v\_LDR}(f)$ that was fitted to both very small and very large values of Illuminance on a LDR sensor. If using the fitted model $E_{v\_LDR}(f)$, for example, to generate a calibration table of a LDR sensor with Multiple-Sensor interface, it would be more pratical to set the values of f<1000Hz as 0 [lx]. On Fig. 41 is visible that for all the experimental dataset of LDR sensor the error of $E_{v\_LDR}(f)$ is always smaller than 30% (except for E_v=0); and the error of $E_{v\_LDR}(f)$ is smaller that 10% for the majority of the experimental dataset.

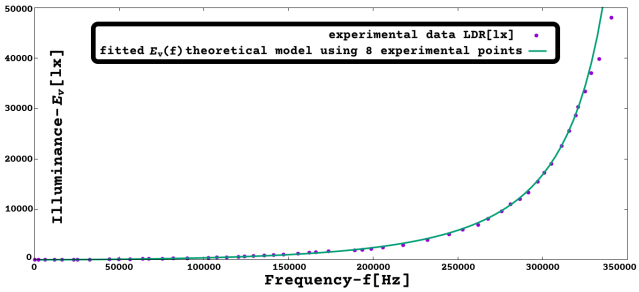

Figure 39: $E_{v\_LDR}(f)$ [lx], with C_1=2.2nF, C_2=2.2nF, frequency in [0Hz, 350kHz] (Sch-trig. osc., Multi-Sensor w. LDR sensor)

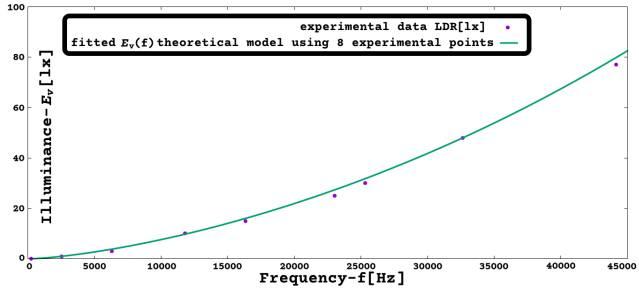

Figure 40: $E_{v\_LDR}(f)$ [lx], with C_1=2.2nF, C_2=2.2nF, frequency in [0Hz, 45kHz] (Sch-trig. osc., Multi-Sensor w. LDR sensor)

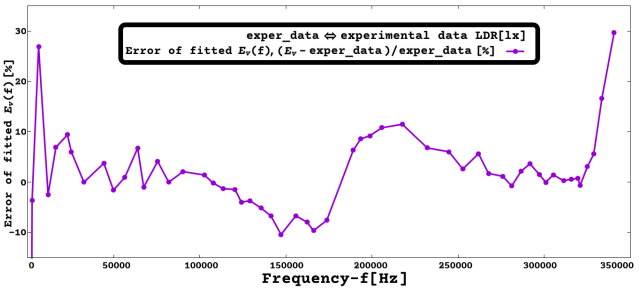

Figure 41: Error of fitted theoretical model $E_{v\_LDR}(f)$, with C_1=2.2nF, C_2=2.2nF

Appendix E. Fluid (ex: water) Level Sensor Dataset

It was made a custom water level sensor (that also may be used for other fluids) that is a planar capacitive sensor made as a double-sided PCB, the sensor may also be used as a soil moisture sensor. For making the sensor as a soil moisture sensor the only physical difference is the shape of the PCB at one of its edges that should be a pointy/triangle shape to make it easier to be buried in the ground, as visible on figure Fig.42 where the pointy/triangle shaped edge is represented by the dashed line.

For adjusting the capacitance of the sensor (C_{sensor}) to the region of C_s(f) of the device that provides a good steady change of frequency versus varying sensor capacitance, was added a 'bias' capacitor (C_{bias}) connected in parallel with the sensing PCB (C_{sense}) that measures fluid level / soil moisture.

The fluid (ex: water) level / soil moisture sensor is a 2 layer PCB (top and bottom layer tracks have exactly the same shape, overlapping PCB tracks are the same circuit node, solder mask acts as insulator), with 6 parallel coplanar capacitive PCB tracks (N_t=6), with dimensions: d_1=120mm, d_2=1.5mm, d_3=2mm, s=1.5mm, w=3mm; and electrical parameters: C_{sense}=45pF (capacitance with air on both sides), if using a bias capacitor of C_{bias}≈1.8nF, then the sensor ca-

pacitance is C_{sensor}≈1.845nF (as seen/measured by the interface device, sensor with air on both sides).

- Reference instruments:

For obtaining the calibration table of the fluid level sensor on the Multiple-Sensor device it was used as a reference a ruler scale laser-printed into transparent plastic film/sheets.

- Jumper Configurations:

[c](JPA on, JPB on): C_1=2.2nF; C_2=2.2nF .

- Units: Hz=hertz, m=meter.

Here is made available a calibration table for the fluid level sensor connected on the Multiple-Sensor Interface and tested with water (fluid), the table shows the water level (h_{water}) versus frequency(f).

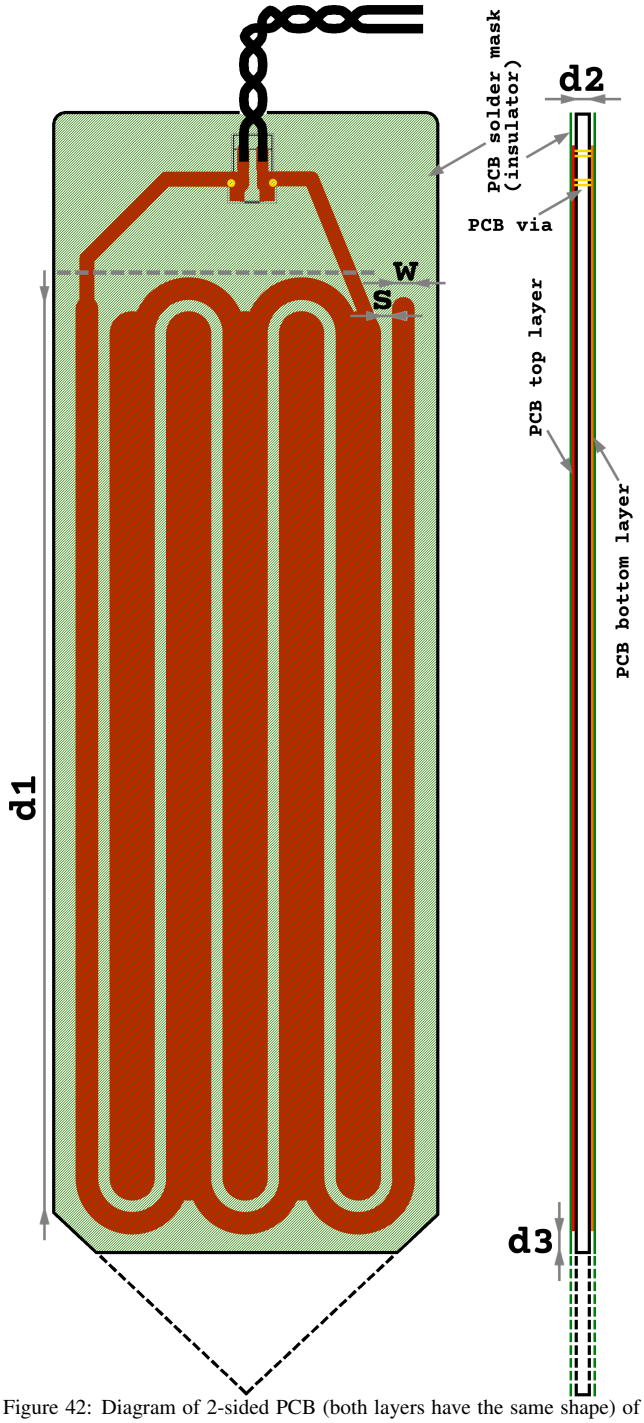

Figure 42: Diagram of 2-sided PCB (both layers have the same shape) of water (or fluid) level sensor or soil moisture sensor (with dashed line edge).

Table 8: Set of exp. data for fluid level sensor (plus C_{bias}≈1.8nF), testing water level [m] vs. frequency [Hz]

h_{water}[m] ref. ruler	f[Hz][c] (sensor) JPA on, JPB on	h_{water}[m] ref. ruler	f[Hz][c] (sensor) JPA on, JPB on
0	269816	0.070	325310
0.005	271244	0.075	328123
0.010	274638	0.080	330875
0.015	281397	0.085	333413
0.020	287686	0.090	336043
0.025	292650	0.095	338505
0.030	296947	0.100	340722
0.035	301044	0.105	342954
0.040	305066	0.110	345049
0.045	308980	0.115	347083
0.050	312420	0.120	348703
0.055	315799	0.125	350125
0.060	319071	0.130	351058
0.065	322282		

Precision error(maximum frequency variation):
±400Hz ($h_{water}\geqslant$0.125m); ±200Hz ($h_{water}<$0.11m)
±300Hz (0.115m$\leqslant h_{water}<$0.125m) .

Appendix F. Fluid (ex: water) Level Sensor Model Fitting and Error

The capacitance of the water level / moisture sensor shown on Fig. 42 can be estimated by the formula of coplanar capacitance; where the copper tracks on the PCB can be described as various straight line coplanar capacitors that are connected at the top and bottom by a curved track.

Also, the straight line coplanar capacitors in the water level / moisture sensor, was modelled as if there was no PCB substrate under the tracks since the overlapping tracks on both sides of the PCB are the same circuit node (they are connected by PCB via/hole), and so overlapping tracks have the same voltage (and so is assumed that between overlapping tracks the electric field is zero); also for the modelling objectives of the sensor made by coplanar capacitors was also assumed that any electric field inside the PCB substrate in the areas not located between overlapping tracks is not relevant compared to the electric field located/concentrated on the air/water/soil over the PCB that is between adjacent copper tracks. Thus the formula of coplanar capacitance [25] (as applied here to straight track pairs surrounded by air/water/soil) can be used (eq. 39), here will be used the approximation that the total track length (d_s) is approximately the length of one of the parallel track segments (d_1) (on the copper zone/area of the PCB) times the number of track segment pairs (N_t) on the PCB (each track segment pair includes top and bottom layer that have the same voltage, and includes + and - terminals of the capacitor), so $d_s \approx N_t d_1$ is an approximation to the total length of the entire copper track from one extremity to the opposite extremity of the same capacitor terminal (+ or -); for example the capacitive sensor on figure Fig. 42 has N_t=6.

$$c_s/d_s = \frac{\varepsilon_r \left(ln \left(\frac{2\left(1+\sqrt[4]{1-(s/(s+2w))^2}\right)}{1-\sqrt[4]{1-(s/(s+2w))^2}} \right) \right)}{377\pi v_0} \quad ,$$
$$0 \leqslant s/(s+2w) \leqslant (1/\sqrt{2}), \quad v_0 = (1/(\sqrt{\varepsilon_0 \mu_0})),$$
Units of '377' constant is [Ω]. (39)

Modelling the fluid level sensor as 2 capacitors in parallel that have different dielectric medium (one capacitor uses air as dielectric the other uses fluid/water as dielectric), where h_{fluid} is the height of the fluid that defines the dimensions of both capacitors, then using equation 39, is possible to write the following equation that relates C_{sense} with h_{fluid}:

$$C_{sense}(h_{fluid}) \approx \frac{(\varepsilon_{r\_fluid} N_t h_{fluid} + (\varepsilon_{r\_air} N_t (d_1 - h_{fluid}))) ln((2(1+\sqrt{k_2}))/(1-\sqrt{k_2}))}{377\pi v_0} \tag{40}$$

The equation 40 can be combined with equation 17 to obtain the following equation, that relates fluid(ex: water) level versus frequency:

$$\begin{aligned}
h_{fluid}(f) &\approx \frac{-377\pi v_0 C_{sense}(f) + (N_t d_1 \varepsilon_{r_air} ln((2(1+\sqrt{k_2}))/(1-\sqrt{k_2})))}{N_t(\varepsilon_{r_air} - \varepsilon_{r_fluid}) ln((2(1+\sqrt{k_2}))/(1-\sqrt{k_2}))}, \\
C_{sense}(f) &= C_{sensor}(f) - C_{bias}, \\
C_{sensor}(f) &\approx \frac{(C_1R_1 + C_2R_2)Hf - 1 - C_1C_2R_1R_2H^2f^2}{Hf((C_1+C_2)R_1R_2Hf - R_1 - R_2)}, \\
v_0 &= (1/(\sqrt{\varepsilon_0 \mu_0})), \\
k_2 &= \sqrt{1 - (s/(s+2w))^2}
\end{aligned} \tag{41}$$

The figures Fig. 43, Fig. 44 are the result of fitting the model function $h_{water}(f) = h_{fluid}(f, \varepsilon_{r\_fluid}{=}\varepsilon_{r\_water})$, to the points: (269816Hz, 0m), (271244Hz, 0.005m), (274638Hz, 0.01m), (287686Hz, 0.02m), (305066Hz, 0.04m), (319071Hz, 0.06m), (330875Hz, 0.08m), (340722Hz, 0.1m), (348703Hz, 0.12m), (351058Hz, 0.13m), and constant (not fitted) parameters d_1=0.12 m, N_t=6 ; obtaining the fitted parameter values: s=0.001284 m; w=0.003457 m; ε_{r_air}=-1.00307; ε_{r_water}=-125.039; H=0.946237; C_{bias}=-3.76339·10^{-9} F; C_1=2.32215·10^{-9} F; C_2=2.45097·10^{-9} F; R_1=1.99478·10^6 Ω; R_2=465.095 Ω.

The fitted values of ε_{r_air}, ε_{r_water}, C_{bias} are negative not because of some model fitting procedure, but were already expected to be negative in accordance with the theoretical analysis where is stated that the capacitive sensor C_{sensor} (or C_s) behaves as negative capacitance when the interface device is operating as Schmitt-Trigger oscillator.

On figure Fig. 45 is shown the relative error in percentage [%] of the fitted model function $h_{water}(f)$ when compared with the full experimental dataset of the water level sensor connected on the Multiple-Sensor interface; the relative error is calculated by subtracting the value of fitted theoretical function ($h_{water}(f)$) from the experimental value of h_{water}, and then dividing by the experimental value of h_{water}. Also is visible that for all the experimental dataset of the water level sensor the error of $h_{water}(f)$ is always smaller than 50%; and the error of $h_{water}(f)$ is smaller that 5% for the majority of the experimental dataset.

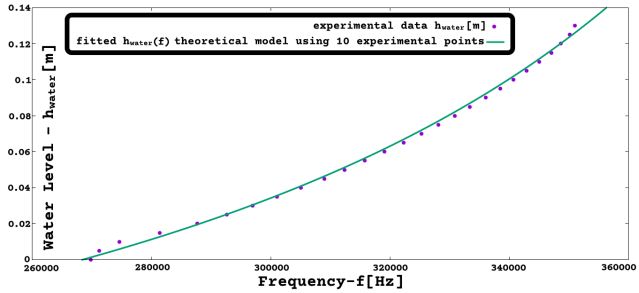

Figure 43: $h_{water}(f)$ [m], with C_1=2.2nF, C_2=2.2nF, frequency in [260kHz, 360kHz] (Sch-trig. osc., Multi-Sensor w. water level sensor)

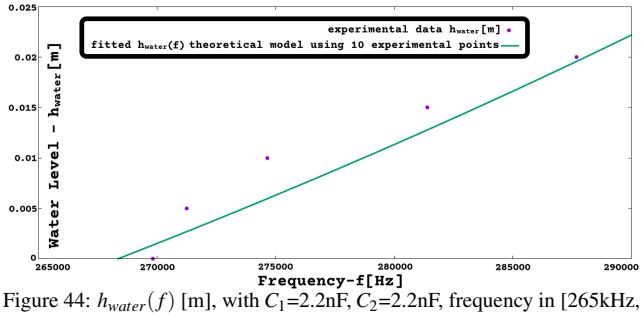

Figure 44: $h_{water}(f)$ [m], with C_1=2.2nF, C_2=2.2nF, frequency in [265kHz, 290kHz] (Sch-trig. osc., Multi-Sensor w. water level sensor)

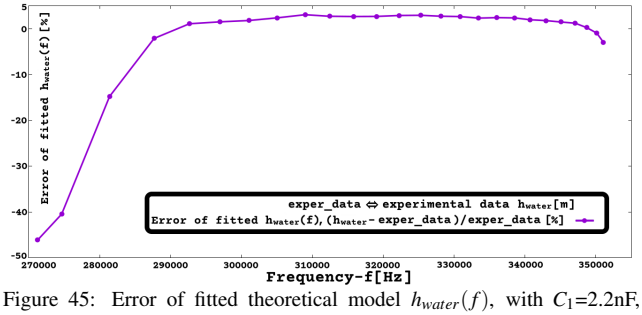

Figure 45: Error of fitted theoretical model $h_{water}(f)$, with C_1=2.2nF, C_2=2.2nF

Appendix G. Abbreviations

ADC . . . . . Analog to Digital Converter
CC BY-NC-SA . . . Creative Commons, Attribution - NonCommercial - ShareAlike
CERN . . . . . Conseil Europeen pour la Recherche Nucleaire
CERN-OHL-W . . . CERN Open Hardware Licence - Weakly reciprocal
CMOS . . . . . Complementary Metal Oxide Semiconductor
EEPROM . . . . . Electrically Erasable Programmable Read-Only Memory
ESD-safe foam . . . Electrostatic Sensitive Device safe foam
FSR . . . . . Force Sensitive Resistor (sensor)
GND . . . . . Ground (voltage reference)
GPIO . . . . . General-Purpose Input/Output
LDR . . . . . Light Dependent Resistor (sensor)
ln(x) . . . . . Natural Logarithm, log_e(x). $ln(e^x) = x$
OCR . . . . . Optical Character Recognition
PCB . . . . . Printed Circuit Board
PWM . . . . . Pulse-Width Modulation
QR-code . . . . . Quick Response code
RS-485 . . . . . Recommended Standard 485 (aka. EIA/TIA-485)
RTD . . . . . Resistance Temperature Detector (sensor)
UART . . . . . Universal Asynchronous Receiver-Transmitter
USB . . . . . Universal Serial Bus
VDD . . . . . Voltage Supply (Voltage Drain Drain)
VDDS . . . . . VDD Stabilized

References

[1] Peter McLean, (2020). Topic 4 - Crystal Oscillators (Pierce oscillator analysis) - Digital Electronics (UTS-AU). Accessed July 2021. https://pmcl.net.au/de .

[2] R.C. Jaeger, T.N. Blalock, (2011). Microelectronic Circuit Design (4th ed.); McGraw–Hill. - '18.6.1 THE COLPITTS OSCILLATOR' p. 1278, '18.6.6 CRYSTAL OS-

CILLATORS' pp. 1283-1285, 'C.2 THE HYBRID OR h-PARAMETERS (Appendix C)' p. 1311 .

[3] A. S. Sedra, K. C. Smith, T. C. Carusone, V. Gaudet, (2021). Microelectronic Circuits (8th inte. ed.); Oxford University Press. - "13.11 LC and Crystal Oscillators" - pp. 1044-1052 .

[4] Eduardo Corpeno - AllAboutCircuits (2018). Exactly How Schmitt Trigger Oscillators Work.
Accessed July 2021.
https://www.allaboutcircuits.com/technical-articles/exactly-how-schmitt-trigger-oscillators-work .

[5] A. O'Neill, D. Appleby, N. Ponon, K. Kwa, (2015). Towards steep slope MOSFETs using ferroelectric negative capacitance. 2014 12th IEEE International Conference on Solid-State and Integrated Circuit Technology (ICSICT). DOI: 10.1109/ICSICT.2014.7021281 .

[6] Andrew K. Jonscher, (1986). The physical origin of negative capacitance. J. Chem. Soc., Faraday Trans. 2, vol. 82, no. 1, pp. 75-81. DOI: 10.1039/F29868200075 .

[7] S. N. Nihtianov, G. P. Shterev, B. Iliev, G. C. M. Meijer, (2001). An interface circuit for R-C impedance sensors with a relaxation oscillator. IEEE Transactions on Instrumentation and Measurement, vol. 50, no. 6, pp. 1563-1567, DOI: 10.1109/19.982945 .

[8] J. H. Lu, M. Inerowicz, S. Joo, J. Kwon, B. Jung, (2011). A Low-Power, Wide-Dynamic-Range Semi-Digital Universal Sensor Readout Circuit Using Pulsewidth Modulation. IEEE Sensors Journal, vol. 11, no. 5, pp. 1134-1144. DOI: 10.1109/JSEN.2010.2085430 .

[9] F.M.L.v.d. Goes, G.C.M. Meijer, (1997). A Universal Transducer Interface for Capacitive and Resistive Sensor Elements. Analog Integrated Circuits and Signal Processing 14, pp. 249–260. DOI: 10.1023/A:1008246103915 .

[10] Xiaowen Liu, D. Rairigh, Chao Yang, A. J. Mason, (2009). Impedance-to-digital converter for sensor array microsystems, 2009 IEEE International Symposium on Circuits and Systems (ISCAS), pp. 353-356, DOI: 10.1109/ISCAS.2009.5117758 .

[11] V. Dumbrava, L. Svilainis, (2007). The Automated Complex Impedance Measurement System. Elektronika Ir Elektrotechnika, 76(4), pp. 59-62. https://eejournal.ktu.lt/index.php/elt/article/view/10720

[12] HIOKI website, (2021). LCR meter basic measurement principles. Accessed December 2021. https://www.hioki.com/global/learning/usage/lcr-meters_1.html .

[13] H. Bi, K. Yin, X. Xie, J. Ji, S. Wan, L. Sun, M. Terrones, M. S. Dresselhaus, (2013). Ultrahigh humidity sensitivity of graphene oxide. Scientific Reports 2013;3:2714. DOI: 10.1038/srep02714 .

[14] C. Yang, A. Mason, J. Xi, P. Zhong, (2006). Configurable Hardware-Efficient Interface Circuit for Multi-Sensor Microsystems. SENSORS 2006 IEEE, pp. 41-44. DOI: 10.1109/ICSENS.2007.355713 .

[15] Thomas Williams, Colin Kelley (2007) - GNUplot software; GNUplot User Manual ver. 6.1, p. 105 . Accessed May 2024. http://gnuplot.sourceforge.net .

[16] Wolfram Research, Inc. - Wolfram Mathematica 12 for Raspberry Pi. 2022. https://www.wolfram.com/raspberry-pi .

[17] Nexperia (NXP, Philips), "74HC14; 74HCT14 - Hex inverting Schmitt trigger - Product data sheet", September 1993 [Rev. 10, 29 February 2024]. https://assets.nexperia.com/documents/data-sheet/74HC_HCT14.pdf .

[18] On-Semi (Motorola), "Hex Schmitt-Trigger Inverter - High-Performance Silicon-Gate CMOS - MC74HC14A, MC74HCT14A" datasheet, Rev. 7 1995 [Rev. 16, March, 2024]. https://www.onsemi.com/download/data-sheet/pdf/mc74hc14a-d.pdf .

[19] Texas Instruments (National Semiconductor), "CD40106B - CMOS Hex Schmitt-Trigger Inverters - SCHS097F" datasheet, November 1998 (February 1988) [revised March 2017]. https://www.ti.com/lit/gpn/cd40106b .

[20] Texas Instruments, "SNx414 and SNx4LS14 Hex Schmitt-Trigger Inverters" datasheet, December 1983 [revised November 2016]. https://www.ti.com/lit/gpn/sn74ls14 .

[21] Excelitas/Perkin-Elmer, "DATASHEET - Photocells A9050, A9060 - Epoxy encapsulated series", 2003 [revised 2011]. https://www.perkinelmer.com/opto .

[22] John R. Taylor, (2022). An Introduction to Error Analysis - The Study of Uncertainties in Physical Measurements (3rd ed.); University Science Books (AIP Publishing). - '3.11 General Formula for Error Propagation' p. 75, 79.

[23] D. C. Baird, (1995). Experimentation - An introduction To Measurement Theory and Experiment Design (3rd ed.); Prentice-Hall Inc. - '2-9 General Method For Uncertainty In Functions Of Two Or More Variables' p.22 .

[24] Do, Trong-Hop, and Myungsik Yoo. (2016). Performance Analysis of Visible Light Communication Using CMOS Sensors. Sensors 16, no. 3: 309, p. 7. 10.3390/s16030309

[25] Clayton R. Paul (2008). Analysis of Multiconductor Transmission Lines (2nd ed.); John Wiley & Sons Inc. - "4.3.1 - Per-Unit-Length Inductance and Capacitance for PCB-Type Lines", pp. 147-148.